

Fabrication and Optimization of Light Emitting Devices with Core-Shell Quantum Dots

by

Katherine Wei Song

B.S.E., Princeton University (2011)

Submitted to the Department of Electrical Engineering and Computer
Science

in partial fulfillment of the requirements for the degree of

Master of Science in Electrical Engineering and Computer Science

at the

MASSACHUSETTS INSTITUTE OF TECHNOLOGY

June 2013

© Massachusetts Institute of Technology 2013. All rights reserved.

Author
Department of Electrical Engineering and Computer Science
March 15, 2013

Certified by
Vladimir Bulović
Professor of Electrical Engineering and Computer Science
Thesis Supervisor

Accepted by
Leslie A. Kolodziejski
Chairman, Department Committee on Graduate Students

Fabrication and Optimization of Light Emitting Devices with Core-Shell Quantum Dots

by

Katherine Wei Song

Submitted to the Department of Electrical Engineering and Computer Science
on March 15, 2013, in partial fulfillment of the
requirements for the degree of
Master of Science in Electrical Engineering and Computer Science

Abstract

Quantum dot light emitting devices (QD-LEDs) are promising options for the next generation of solid state lighting, color displays, and other optoelectronic applications. Overcoating quantum dots (QDs) – semiconducting nanocrystals of CdSe, PbS, or another similar compound – with a wide band-gap “shell” has recently been shown to significantly boost QD-LED performance and yield the most efficient QD-LEDs to date. This thesis studies fabrication techniques to make bright, efficient QD-LEDs with these “core-shell” QDs. The first part studies the electrophoretic deposition (EPD) of CdSe/ZnS QDs. QD-LEDs conventionally utilize a QD film that is deposited via spin-casting, a reliable but highly unscalable technique for the deposition of thin, smooth films of QDs for QD-LED applications. Potential advantages of EPD include the ability for deposition onto a variety of substrate shapes and more energetically favorable QD packing. Devices made with EPD QD films exhibit peak efficiencies comparable to those of devices with a spun-cast QD layer and turn-on voltages surprisingly lower than the optical band-gap of the QDs. These results suggest that EPD is a viable alternative to spin-casting for the processing of QD-LEDs.

The second part of this thesis explores the role of core-shell QDs in creating bright, efficient LEDs in the near-infrared ($\lambda > 1 \mu\text{m}$) regime. Infrared QD-LEDs with record brightness and efficiencies are obtained by using QDs in which lead sulfide (PbS) cores are overcoated with a cadmium sulfide (CdS) shell. *In situ* photoluminescence quantum yield measurements confirm that the QD shell plays a significant role in shielding the emissive QD core from external quenching mechanisms.

Finally, fabrication and material considerations for the non-QD layers in the modern QD-LED structure are also discussed. This thesis analyzes different film formation techniques for zinc oxide (ZnO), the electron transport layer in the QD-LEDs, and different materials and thicknesses for the organic hole transport layer.

Thesis Supervisor: Vladimir Bulović
Title: Professor of Electrical Engineering and Computer Science

Acknowledgments

I am indebted to my advisor, Vladimir Bulović, whose support and endless enthusiasm made this work possible and broadened my perspectives as a scientist. I am also grateful for the scientific and moral support from all the members of the Organic and Nanostructured Electronics Laboratory (ONE Lab). I would especially like to thank Yasuhiro Shirasaki and Geoffrey Supran, the group's resident quantum dot light emitting device experts, for patiently sharing their wisdom with me in the past 2 years, and Farnaz Niroui for always being there to help me sort through an endless jumble of ideas about research and life. Additional acknowledgements go to the MIT Henry Ford II Fellowship, the NSF Graduate Research Fellowship, and the DOE Center for Excitonics for generously funding my work.

Finally, I am forever thankful for the many other wonderful people who helped me find my way (and survive) to where I am, including but not limited to my undergraduate research advisors, Sigurd Wagner and Naveen Verma, my mother, and everyone else who has ever made me think or laugh.

Contents

1	Introduction	15
1.1	Progress in light emitting technologies	15
1.2	Colloidal quantum dots	19
1.2.1	Basic concept	19
1.2.2	QD synthesis overview	20
1.2.3	Core-shell QDs	21
1.3	Thesis overview	22
2	Operation of QD-LEDs	23
2.1	Hybrid QD-LED architecture	23
2.2	Charge transport in organic semiconductors	24
2.3	Light emission in QD-LEDs	25
2.4	Device evaluation	27
2.4.1	Photoluminescence and electroluminescence spectra	27
2.4.2	Efficiency and brightness	27
3	Electrophoretic Deposition of CdSe/ZnS Quantum Dots	31
3.1	Motivation	31
3.2	Methods	33
3.2.1	Fabrication of QD-LEDs	33
3.2.2	Electrophoretic deposition procedure	34
3.3	Film characterization	36
3.3.1	Roughness and thickness	36

3.3.2	Photoluminescence of anode versus cathode	38
3.4	Optically patterning films	39
3.5	Device performance	40
3.6	Summary	46
4	Near-Infrared QD-LEDs	49
4.1	Motivation	49
4.2	Methods	50
4.2.1	Synthesis of core-shell PbS/CdS NIR QDs	50
4.2.2	Fabrication of NIR QD-LEDs	52
4.3	Efficiency and brightness of PbS/CdS QD-LEDs	53
4.4	Linking EQE and PL quantum yield	55
4.5	Summary	58
5	Optimization of Charge Transport Layers in QD-LEDs	59
5.1	Electron transport layer	59
5.2	Hole transport layer	61
5.2.1	The “matted” phenomenon	61
5.2.2	Material selection	64
5.2.3	Microcavity effect	67
5.3	Hole injection layer	70
5.4	Summary	72
6	Conclusion	73
A	Detailed fabrication procedures	75
A.1	QD crash-out	75
A.2	Cleaning substrates	75
A.3	Sol-gel processing of ZnO	76
A.4	Evaporation of HTL, HIL, and anode	77

List of Figures

1-1	Photograph (courtesy: Felice Frankel) of QD solutions photoluminescing under excitation with an ultraviolet lamp.	17
1-2	CIE chromaticity diagram showing the color saturation capabilities of QD-LEDs (courtesy of [1]).	18
1-3	Schematic of three-neck flask synthesis of colloidal quantum dots.	20
2-1	“Hybrid” QD-LED structure.	24
2-2	Exciton formation mechanisms in QDs. From top to bottom: optical excitation (e.g. with a blue laser), Förster resonant energy transfer (FRET), and direct charge injection. A photon is emitted when the exciton radiatively recombines.	26
2-3	1924 CIE standard luminosity function.	30
3-1	Schematic cross section of the QD-LED structure used for EPD and control devices (left) and the corresponding flat-band energy diagram (right) with energy levels taken from literature [2, 3, 4, 5, 6].	33
3-2	Schematic of a 2-step electrophoretic deposition process for the formation of thin, luminescent QD films.	35
3-3	Current through EPD setup versus time.	36
3-4	AFM topography image of EPD QDs on a ZnO-on-ITO anode. EPD lasted for 5 minutes under a 20 V applied bias (electric field of 50 V/cm).	37
3-5	Step profile of scratch in an anodic EPD QD film (5 minute deposition under a field of 50 V/cm) showing a film thickness of 15 nm.	38

3-6	Photographs of anode (+) and cathode (-) of EPD QD films on FTO electrodes under ambient light (left) and in the dark under a UV lamp (right) demonstrating that a more photoluminescent film forms on the cathode.	39
3-7	Energy dispersive X-ray spectroscopy map of the edge of the dark spot on the cathode shown in Figure 3-6. Green pixels mark the presence of Zn, yellow pixels mark the presence of S, and teal pixels mark the presence of Sn (from the underlying FTO).	40
3-8	Photograph of EPD cathode photoluminescence under a UV lamp. The position of the darkened line (marked by an arrow) is in agreement with the placement of a line of green laser light shone onto the substrate during EPD.	41
3-9	10 simultaneously lit devices operating at approximately 100 cd/m ²	41
3-10	Current density versus voltage for QD-LEDs with an EPD QD layer (red) and a spun-cast QD layer (black).	42
3-11	Photodetector current versus voltage for QD-LEDs with an EPD QD layer (red) and a spun-cast QD layer (black).	43
3-12	External quantum efficiency versus current density for QD-LEDs with a spun-cast QD layer, a dip-coated QD layer, and various EPD QD layers.	44
3-13	Electroluminescence spectra for QD-LEDs operating at ~ 100 Cd/m ² . The photoluminescence spectrum of the starting QD solution is provided for reference.	45
3-14	Electroluminescence peak wavelengths for EPD QD-LEDs with different EPD conditions. The red line indicates the peak wavelength of control QD-LEDs (with a 10 nm spun-cast QD layer). EPD anode devices lie in the positive voltage half of the plot (right), and the EPD cathode devices lie in the negative voltage half of the plot (left).	46
4-1	Schematic of a cation exchange process for the growth of a CdS shell on PbS QDs.	51
4-2	Cross-section schematic of NIR QD-LEDs and the corresponding flat-band energy diagram, with energy levels taken from literature [2, 3, 4, 5, 6].	52

4-3	Current density vs. voltage curves for QD-LEDs made with core-shell PbS/CdS (shell thickness = 0.21 nm) QDs (red) and with core-only PbS QDs (black).	53
4-4	Radiance vs. voltage curves for QD-LEDs made with core-shell PbS/CdS (shell thickness = 0.21 nm) QDs (red) and with core-only PbS QDs (black).	54
4-5	External quantum efficiency vs. current density curves for QD-LEDs made with core-shell PbS/CdS (shell thickness = 0.21 nm) QDs (red) and with core-only PbS QDs (black).	55
4-6	External quantum efficiencies (red) for QD-LEDs made with various QDs (including core-only and core-shell QDs with varying shell thickness) overlaid on trends in relative η_{PL} measured for bulk QD films (black) and for 8 nm QD films sandwiched between ZnO and CBP (blue).	57
5-1	Image of dry-air-filled glovebag used to anneal ZnO during sol-gel processing.	61
5-2	Surface of top gold electrode of a “normal” NIR QD-LED (left) and a “matted” NIR QD-LED (right).	62
5-3	Cross sections of a “normal” NIR QD-LED (left) and a “matted” NIR QD-LED (right).	63
5-4	Zoomed-in cross sections of a “normal” NIR QD-LED (left) and a “matted” NIR QD-LED (right) showing that the roughness of the latter originates from the impartial formation of CBP islands.	63
5-5	Current density versus voltage curves for QD-LEDs made with different HTLs (each is 100 nm thick).	65
5-6	Photodetector current versus voltage for QD-LEDs made with different HTLs (each is 100 nm thick).	66
5-7	EQE versus current density for QD-LEDs made with different HTLs (each is 100 nm thick).	66
5-8	Current density versus voltage curves for QD-LEDs made with: a 100 nm CBP HTL + 10 nm MoO _x HIL (black), a 150 nm CBP HTL + 10 nm MoO _x HIL (blue), and a 100 nm CBP HTL + 60 nm MoO _x HIL (red).	68

List of Tables

3.1 Electroluminescence peak and width of control and EPD QD-LEDs	45
A.1 Sublimation conditions (for QD-LED HTL, HIL, and anode)	77

Chapter 1

Introduction

1.1 Progress in light emitting technologies

Since the invention of the incandescent light bulb in the 19th century, the evolution of lighting technologies has been guided by the often competing demands for longer lifetimes, higher efficiencies, lower costs, and better color rendering. Inorganic light emitting diodes (LEDs) [7], consisting of a p-n junction formed by films of two inorganic semiconductors, boast improvements over former generations of lighting in terms of lifetimes and efficiencies, but their high cost currently limits their realization to niche, small-area applications in solid state lighting [8]. In 1987, over half a century after the first inorganic LED was invented [7], Kodak demonstrated the first organic light emitting diode (OLED) [9], a device whose lack of high-temperature and high-vacuum processing requirements promise an economical lighting alternative to their inorganic predecessors. Although the efficiencies and air stability of OLEDs still lag behind those of their inorganic counterparts, their potentially low manufacturing cost, mechanical flexibility, light weight, and wide viewing angle make OLEDs especially attractive for large area displays, a market currently dominated by liquid crystal displays (LCDs) [10, 11, 12, 13, 14]. Unlike LCDs, color OLED displays require no backlight, polarizers, or filters, paving the way for lighter and lower-power displays. With massive improvements in efficiencies, color saturation, brightness, and encapsulation seen in recent years, OLEDs are finally beginning to see widespread

commercial realization.

The quantum dot LED (QD-LED), the focus of this thesis, was born in the 1990s when Colvin *et al.* embedded quantum dots (QDs) in a polymer matrix sandwiched between two metal electrodes and observed electroluminescence upon applying a voltage to the electrodes [15]. The QD-LED has evolved greatly since its inception, and as will be discussed in Chapter 2, modern QD-LED architectures are derived from the more complex multi-layer structure of conventional OLEDs. QD-LEDs benefit from many of the same perks of OLEDs, including solution processability, the potential for low cost, and high color saturation. Multicolor QD-LEDs on plastic substrates that remain operational under bending down to a ~ 5 mm radius of curvature have been demonstrated, highlighting QD-LEDs' capability for use in lightweight, flexible applications [16]. Furthermore, multiple large-area processing techniques, such as mist-deposition [17], ink-jet printing [18], and contact printing [19], have been reported, showcasing the many options for the economical fabrication of QD-LEDs. In terms of performance, QD-LEDs are rapidly approaching their OLED predecessors. In 2013, QD Vision reported QD-LEDs with an external quantum efficiency (EQE) of 18%, a value comparable to those of phosphorescent OLEDs [20]. These devices exhibited brightnesses greater than 50000 Cd/m^2 , a luminous efficiency of 19 Cd/A , and an estimated internal quantum efficiency of 90%.

One significant perk of QD-LEDs in comparison to OLEDs is that whereas the viable emission range of OLEDs is restricted to approximately one third of the visible spectrum due to the limited availability of small band-gap organic dyes [21], QD emission is tunable over the entire visible to near-infrared spectrum, as partially demonstrated by Figure 1-1, a photograph showing the photoluminescence under ultraviolet light of various size QDs in solution [1]. As will be discussed later in this chapter, tuning the emission of QDs can in theory be accomplished simply by controlling the QDs' size during synthesis – a much more straightforward task than tuning the emission spectrum of organic dyes.

One consequence of QDs' tunability is that QD-LEDs are capable of achieving a more complete color gamut and a more natural white light than existing technologies



Figure 1-1: Photograph (courtesy: Felice Frankel) of QD solutions photoluminescing under excitation with an ultraviolet lamp.

[1]. The Commission International de l'Eclairage (CIE) chromaticity diagram of Figure 1-2 plots the gamut of human vision and shows that QD-LEDs are capable of achieving highly saturated colors that exceed current standards for high-definition displays. Each color with a spectral power distribution $I(\lambda)$ (where λ is wavelength) in the CIE color space is defined by the tristimulus values X, Y, and Z, where

$$\begin{aligned} X &= \int_{380}^{780} I(\lambda) \bar{x}(\lambda) d\lambda \\ Y &= \int_{380}^{780} I(\lambda) \bar{y}(\lambda) d\lambda \\ Z &= \int_{380}^{780} I(\lambda) \bar{z}(\lambda) d\lambda \end{aligned} \quad (1.1)$$

In the above expressions, $\bar{x}(\lambda)$, $\bar{y}(\lambda)$, and $\bar{z}(\lambda)$ are color-matching functions that represent the 3 spectral sensitivity curves in humans. Each color in Figure 1-2 is then specified by the 2 coordinates x and y as:

$$x = \frac{X}{X + Y + Z} \quad (1.2)$$

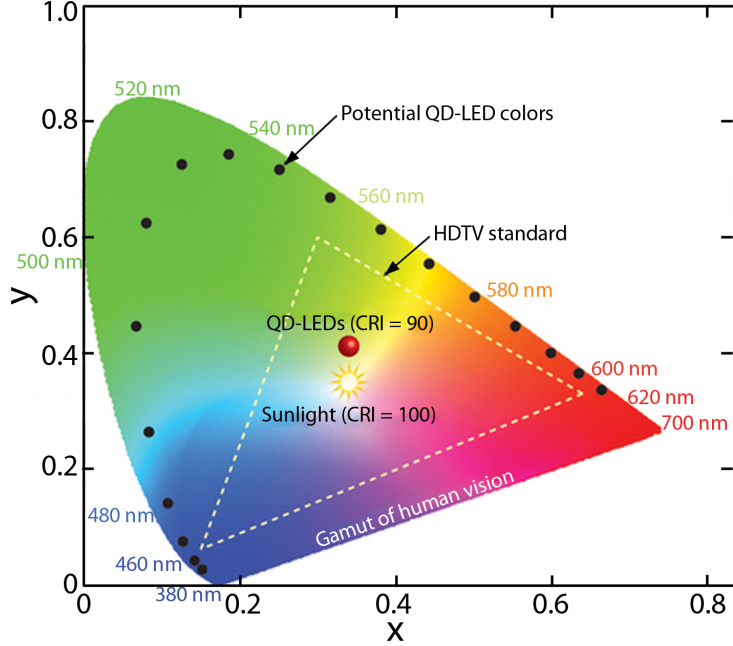


Figure 1-2: CIE chromaticity diagram showing the color saturation capabilities of QD-LEDs (courtesy of [1]).

$$y = \frac{Y}{X + Y + Z}$$

Furthermore, this emission tunability makes QD-LEDs especially attractive for applications requiring emission in the infrared, a regime currently dominated by inorganic light emitters due to the lack of economical, high-performance OLED alternatives. QDs made from small band-gap lead chalcogenides, such as lead sulfide (PbS) and lead selenide (PbSe), can be readily used to produce infrared QD-LEDs with external quantum efficiencies (EQEs) greater than 1% at tunable emission wavelengths above $1\mu\text{m}$. The development of even more efficient infrared QD-LEDs will be discussed in more detail in Chapter 4.

The rest of this chapter provides an introduction to the concept of colloidal quantum dots, a critical building block of QD-LEDs. Section 1.2 provides a basic explanation of the optical properties and synthesis procedure of colloidal QDs. Section 1.3 provides an overview for the rest of this thesis.

1.2 Colloidal quantum dots

1.2.1 Basic concept

The term “quantum dot” (QD) in this thesis refers to a spherical nanocrystal with a radius smaller than the exciton (a bound electron hole pair) Bohr radius, $a_B = \frac{4\pi\hbar^2}{\mu\epsilon^2}$, where ϵ is the permittivity of the material and μ is the reduced mass of the exciton ($\frac{1}{\mu} = \frac{1}{m_e^*} + \frac{1}{m_h^*}$, where m_e^* and m_h^* are the electron and hole effective masses, respectively). The energy levels of a quantum dot are determined by quantum confinement effects, which are responsible for the discrete energy levels that allow for QDs’ narrow emission spectra. In the most basic model, an electron or hole may be represented as a particle in a spherical well surrounded by an infinite potential. The energy of such a particle of mass m in a sphere of radius a is obtained from solving the time-independent Schrödinger equation,

$$E\Psi(\mathbf{r}) = -\frac{\hbar^2}{2m}\nabla^2\Psi(\mathbf{r}) + V(\mathbf{r})\Psi(\mathbf{r})$$

where $V = 0$ inside the QD and $V = \infty$ outside the QD. The eigen-energies of such a system are described by

$$E_{n,l} = \frac{\hbar^2 k_{n,l}^2}{2m} = \frac{\hbar^2 z_{n,l}^2}{2ma^2} \quad (1.3)$$

where $z_{n,l}$ is the n th root of the l th order Bessel function. The energy of a bound electron-hole (exciton) state can then be approximated as the band gap of the bulk semiconductor material, E_g , corrected by the electron and hole energies from Equation 1.3 and $-\frac{1.8e^2}{\epsilon a}$, the first-order correction term to account for the Coulombic attraction between the electron and hole (where the coefficient is approximated numerically adding a first-order Coulombic perturbation to the 3D spherical well problem):

$$E = E_g + \frac{\hbar^2}{2a^2} \left(\frac{z_{n_h,l_h}^2}{m_h^*} + \frac{z_{n_e,l_e}^2}{m_e^*} \right) - \frac{1.8e^2}{\epsilon a} \quad (1.4)$$

Equation 1.4, while being far from providing a complete quantitative representation of band edges in QDs, offers elementary intuition for factors affecting the energy emitted

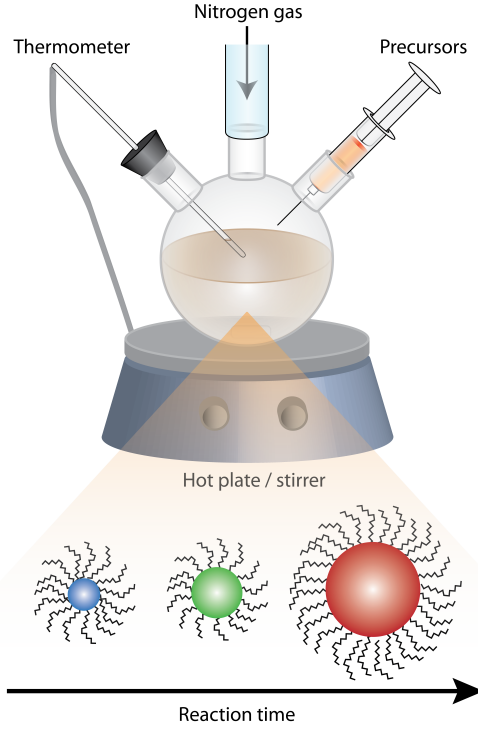


Figure 1-3: Schematic of three-neck flask synthesis of colloidal quantum dots.

from a QD during the radiative recombination of an electron-hole pair and demonstrates that emission energy may be tuned by changing the QD material (materials with wider band-gaps E_g lead to higher emission energies and thus bluer emission) or the QD size (QDs with smaller radii a have bluer emission).

1.2.2 QD synthesis overview

QDs can be made epitaxially ([22]) or colloidally ([23, 24]). In epitaxial synthesis, a semiconductor material is often grown via a layer by layer vapor phase technique in a manner that induces a great amount of strain (e.g. growing a film on a substrate with a very different lattice constant). At a critical thickness that depends on the material set, the built-up strain causes the deposited layer to nucleate and form quantum dot islands. In addition to being financially costly, this method does not offer straightforward QD shape and size tunability and fails to produce QDs with high photoluminescence (PL) quantum yields (QYs), an important metric in producing efficient QD-LEDs.

On the other hand, colloidal QD synthesis yields QDs that are monodisperse, possess a high PL QY, and are solution processable. Such advantages allow for cheaper, more efficient, and brighter QD-LEDs, making the choice of colloidal QDs in this work a natural selection. Colloidal QDs are typically made via solution synthesis in a three-neck flask, as shown in Figure 1-3 [23]. Nucleation begins when organometallic precursors, such as dimethylcadmium [Me_2Cd] and bis(trimethylsilyl)selenium [$(\text{TMS})_2\text{Se}$] in the case of CdSe QDs, are injected into a pre-heated flask containing an organic solvent with ligands, such as tri-*n*-octylphosphine oxide (TOPO), to solubilize the QDs. As QDs begin to nucleate, the temperature of the solution drops, slowing growth. The solution is then heated until the desired QD size, which can be carefully tuned by controlling the time and temperature of the reaction, is reached. Typically, the QDs are then “crashed out” (precipitated and dried, as detailed in Appendix A) of the synthesis solution and subsequently redispersed into a clean solvent. This may be done multiple times to remove excess ligands in the solution.

Red-orange QDs used in this work are provided by QD Vision Incorporated. Infrared QDs are fabricated by Gyuweon Hwang in the Bawendi Lab at MIT.

1.2.3 Core-shell QDs

The most efficient QD-LEDs to date rely on “core-shell” QDs – dots whose emissive cores are surrounded by a wider band-gap shell, such as CdS, ZnS, or ZnSe. Surface defects on core-only QDs are responsible for deep trap states that form non-radiative relaxation pathways. Along with stabilizing QDs by hindering oxidation, the addition of a shell confines excitons to the radiative QD core, boosting PL QY [25]. The benefits derived from using core-shell QDs in place of core-only QDs in QD-LEDs will be highlighted in Chapter 4.

There are several methods to form core-shell QDs via colloidal synthesis. One common method is to slowly add shell precursors, such as diethylzinc [ZnEt_2] and hexamethyldisilathiane [$(\text{TMS})_2\text{S}$] (to form ZnS) to a heated flask containing core-only QDs with ligands and organic solvent in an N_2 atmosphere [25]. In this method, shell growth onto the QD cores proceeds via a similar mechanism as core growth

does in the standard QD synthesis procedure. Another approach, discussed in more detail in Chapter 4, is cation exchange, during which the QD cation (e.g. Pb^{2+}) is displaced by another cation (e.g. Cd^{2+}) in solution [24, 26]. This method is particularly useful for near-infrared lead chalcogenide QDs, for which standard shell growth is energetically unfavorable.

1.3 Thesis overview

Chapter 2 addresses the structure and operational principles of the “modern” QD-LED structure used in this thesis. Chapters 3 and 4 discuss studies related to the QD layer. In particular, Chapter 3 focuses on the development of an electrophoretic deposition (EPD) technique for the formation of thin, luminescent CdSe/ZnS QD films that can be used to make efficient QD-LEDs. Chapter 4 demonstrates how replacing PbS QDs with core-shell PbS/CdS QDs enables the development of bright and efficient QD-LEDs emitting in the near-infrared. Chapter 5 discusses various possible optimizations of layers other than the QD layer in the QD-LED structure. It investigates different film formation techniques for zinc oxide (ZnO), the QD-LED electron transport layer, different candidates for the QD-LED hole transport layer, and the significance of a metal oxide hole injection layer. Finally, Chapter 6 summarizes the main contributions of this thesis.

Chapter 2

Operation of QD-LEDs

2.1 Hybrid QD-LED architecture

Although invented less than twenty years ago, QD-LEDs have already seen several generations of device architectures [1]. Shortly after the first QD-LED [15], which was composed of a QD-polymer blend between two electrodes, was reported, Coe *et al.* demonstrated an alternative QD-LED architecture by embedding a QD monolayer between two organic charge transport layers in a conventional OLED stack [27]. The architecture that has produced the most efficient QD-LED reported to date is a “hybrid” structure that derives from Coe’s work. In this so-called “Type IV,” or inorganic-QD-organic architecture, a thin layer of QDs is sandwiched between an inorganic, metal oxide electron transport layer and an organic hole transport layer, as shown in Figure 2-1 [1]. This multilayer structure is sandwiched between a reflective conducting electrode and a transparent one, through which light is emitted and collected.

To promote efficient charge injection, there is ideally no energy barrier for electrons to flow from the anode through the electron transport layer (ETL) to the QD layer, and there is a large barrier for holes. Red-orange CdSe QDs have an approximate highest occupied molecular orbital (HOMO) energy level of 6.6 eV below the vacuum level and an approximate lowest unoccupied molecular orbital (LUMO) energy level of 4.4 eV below the vacuum level. A typical material choice for the ETL is zinc oxide

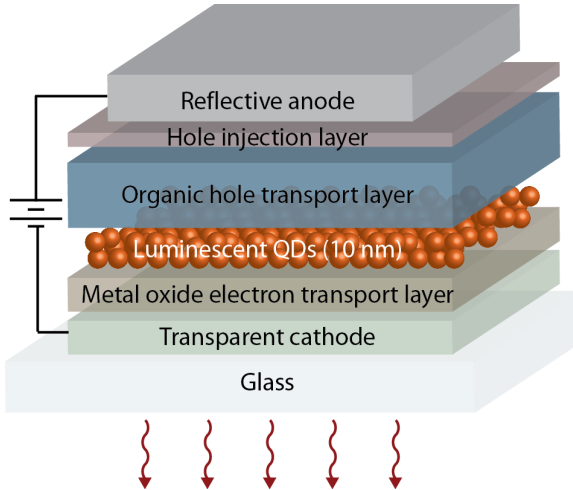


Figure 2-1: “Hybrid” QD-LED structure.

(ZnO), which has approximate band edges of 7.4 eV and 4.2 eV below the vacuum level [4]. Likewise, in an ideal hole transport layer (HTL), there is no energy barrier for holes to flow from the anode to the QD layer, and there is a large barrier for electrons. One possible choice for such a material is (4,4'-N,N'-dicarbazole)biphenyl (CBP), which has approximate HOMO and LUMO energies of 6.0 eV and 4.0 eV below the vacuum level, respectively [3]. More details about the choice of these layers will be discussed in Chapter 5.

2.2 Charge transport in organic semiconductors

A wide band-gap organic semiconductor is used as a hole-transporting layer in a hybrid “Type IV” QD-LED structure. Such organic molecules possess alternating single and double carbon-carbon bonds that form a π -conjugated system, leading to delocalization of an electron and giving rise to a “band-gap” (e.g. 3 eV) between the HOMO, a π orbital, and the LUMO, a π^* antibonding orbital. Organic molecules are bound to one another by weak van der Waals interactions, and charge transfer between molecules must occur via a hopping mechanism, whereby electrons hop between LUMOs and holes hop between HOMOs of neighboring molecules (there is evidence for band-like transport that occurs in more ordered organic semiconductors

in which there is significant overlap of π orbitals among molecules, but this will not be discussed here). Thus, the mobilities of organic semiconductors tend to be lower than those of crystalline inorganic semiconductors, in which charges move through regular lattices formed by covalent bonds between atoms. Whereas mobility in crystalline inorganic semiconductors is limited at high temperature by lattice vibrations that scatter electrons, hopping is a temperature-assisted mechanism, so mobility increases with temperature in disordered organic semiconductors and other materials in which the hopping mechanism dominates.

The low conductivity of organic semiconductors, while unfavorable for high-speed applications, makes them a good candidate for a charge transport layer for QD-LEDs, because they have a smaller PL quenching effect on QDs than metal oxides with higher conductivities [28].

2.3 Light emission in QD-LEDs

A QD can be induced to emit light when an exciton (bound electron-hole pair) forms in the QD and recombines to emit a photon. Three mechanisms for exciton formation on QDs are represented schematically in Figure 2-2. An exciton may be formed via optical or electrical excitation. The former, in which a high-energy photon is absorbed by the QD to form an exciton, is responsible for photoluminescence, while the latter is responsible for QD-LED operation. While some debate still exists, much evidence points toward direct charge injection and Förster resonant energy transfer (FRET) as two significant exciton-formation mechanisms present in a hybrid QD-LED architecture [1, 29]. There is little agreement as to which mechanism dominates and whether the mechanisms are competing or independent [29].

In the case of direct charge injection, an exciton forms when an electric field drives the injection into a QD of an electron and a hole from separate charge transport layers on either side of a QD. In the case of FRET (sometimes simply called energy transfer), an exciton forms in the wide band-gap organic hole transport layer and non-radiatively transfers its recombination energy via dipole-dipole interactions to a

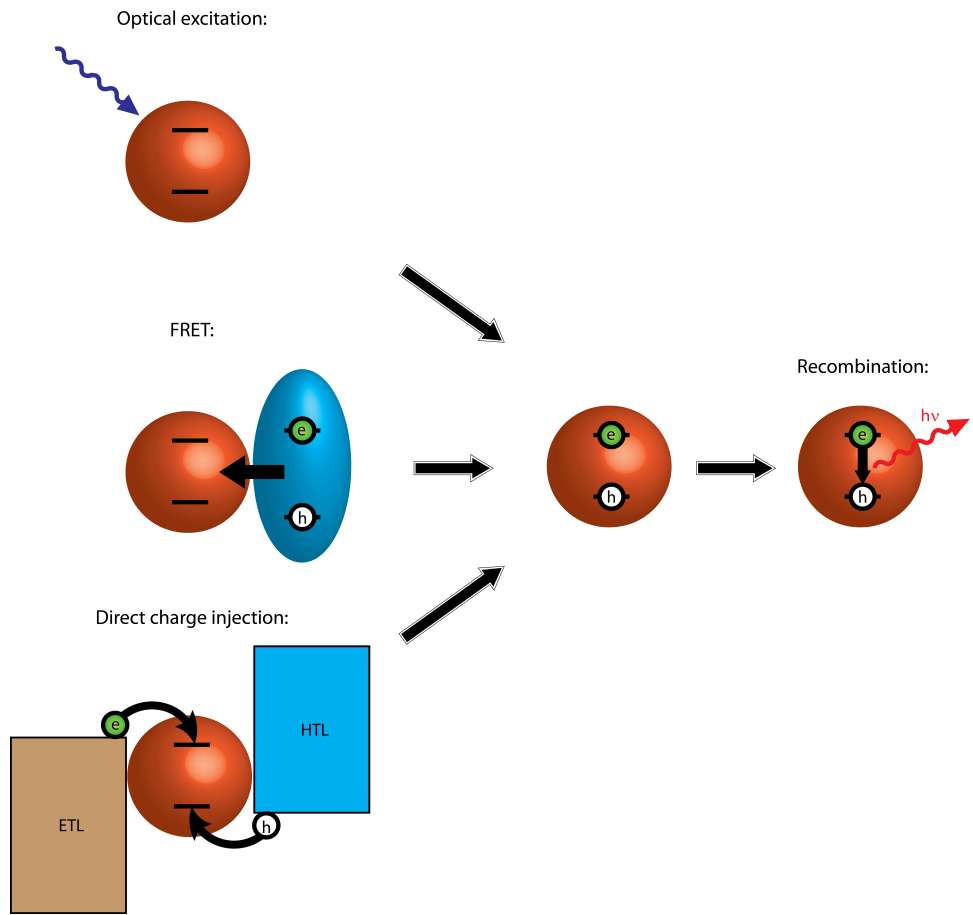


Figure 2-2: Exciton formation mechanisms in QDs. From top to bottom: optical excitation (e.g. with a blue laser), Förster resonant energy transfer (FRET), and direct charge injection. A photon is emitted when the exciton radiatively recombines.

QD, forming an exciton on the QD. The critical distance for FRET, known as the Förster radius, is ~ 10 nm for a typical QD-organic system [30]. Regardless of the mechanism of exciton formation, a photon is emitted when the exciton formed on a QD radiatively recombines.

2.4 Device evaluation

2.4.1 Photoluminescence and electroluminescence spectra

Photoluminescence (PL) spectra are measured by optically exciting a material or device and measuring the emission spectrum (intensity vs. wavelength) using a spectrometer. Electroluminescence (EL) spectra are measured in a similar way, but exciton formation and recombination is driven by electrical, not optical, excitation. By comparing the EL spectrum of a QD-LED to the PL spectra of the individual layers in the device, the contribution of the different layers to device emission can be determined. As will be discussed in the next section, the EL spectrum is also important for evaluating the brightness and efficiency of a QD-LED.

2.4.2 Efficiency and brightness

Standard QD-LED testing consists of measuring current density as a function of voltage ($J - V$ curves), light output power as a function of voltage ($L - V$), and the electroluminescence spectrum (EL) under an applied voltage above the turn-on voltage of the device. Testing is done in a nitrogen-filled glovebox or after packaging the devices with Torr Seal ultra-high-vacuum epoxy. $J - V$ curves are obtained simply by sweeping the voltage applied between the cathode and anode of the device and measuring the current passing through these terminals with a Keithley 2636A current/voltage sourcemeter. Current density, J , is related to voltage, V , by:

$$J \propto V^{n+1} \quad (2.1)$$

where n , the slope of the $J - V$ curve on a log-log scale, depends on the dominant conduction mechanism. Generally, $n = 0$ is characteristic of ohmic conduction, and $n > 1$ is characteristic of trap-limited conduction [31].

$L - V$ curves are obtained by using a Newport Multi-Function Optical Meter 1835-C to record the current passing through a calibrated photodiode (Si for visible wavelengths and Ge for infrared wavelengths) that is placed above the device as $J - V$ curves are collected. From this photocurrent, the light output power detected by the photodetector at a given wavelength, $l(\lambda)$, is estimated as

$$l(\lambda) = \frac{I_{pc}}{R_{pd}(\lambda)} [W] \quad (2.2)$$

where $R_{pd}(\lambda)$ is the responsivity of the photodetector ([A/W]) at a wavelength λ . For a given EL spectrum, S , the total light output power, L , is then found by integrating the contributions from different emission wavelengths as

$$L = \frac{G}{\int_{380}^{780} S(\lambda) d\lambda} \int_{380}^{780} l(\lambda) S(\lambda) d\lambda = \frac{G \times I_{pc} \int_{380}^{780} \frac{S(\lambda)}{R_{pd}(\lambda)} d\lambda}{\int_{380}^{780} S(\lambda) d\lambda} [W] \quad (2.3)$$

where G is the geometric gong factor to account for the fact that only a fraction of the total emitted power is collected by the small photodetector. Assuming Lambertian emission, it is determined as

$$G = \frac{r_{pd}^2}{r_{pd}^2 + d^2} \quad (2.4)$$

where r_{pd} is the radius of the active area of the photodetector and d is the distance from the front of the device to the photodetector.

L is often more simply estimated as GI_{pc}/R_{peak} , where R_{peak} is the responsivity of the photodetector at the peak EL wavelength. From here, the number of photons generated by the device per second is

$$N_{photon} = \frac{L}{E_{photon}} \quad (2.5)$$

where E_{photon} is the photon energy (hc/λ , where h is Planck's constant and c is the

speed of light). E_{photon} can simply be taken as the photon energy for the peak EL wavelength, or, more rigorously, N_{photon} can be rewritten as

$$N_{photon} = \frac{G \times \int_{380}^{780} \frac{l(\lambda)}{E_{photon}(\lambda)} S(\lambda) d\lambda}{\int_{380}^{780} S(\lambda) d\lambda} = \frac{G \times I_{pc} \int_{380}^{780} \frac{\lambda S(\lambda)}{R_{pd}(\lambda)} d\lambda}{hc \int_{380}^{780} S(\lambda) d\lambda} \quad (2.6)$$

External quantum efficiency (EQE) is defined as ratio of photon current to electron current and is calculated from N_{photon} and I , the current through the device ([A]) as

$$EQE = \frac{N_{photon}}{N_{electron}} = \frac{N_{photon}}{I/1.6 \times 10^{-19}} \times 100\% \quad (2.7)$$

Luminous flux, Φ_v ([lm]), quantifies the power of light perceived by the human eye. Given a normalized spectral power distribution, $J(\lambda)$ ([W]) = $\frac{\frac{G \times I_{pc}}{R_{pd}(\lambda)} S(\lambda)}{\int_{380}^{780} S(\lambda) d\lambda}$, it is calculated as follows:

$$\Phi_v = 683[lm/W] \times \int_{380}^{780} \bar{y}(\lambda) J(\lambda) d\lambda \quad (2.8)$$

where A_{LED} is the area of the LED and $\bar{y}(\lambda)$ is the 1924 CIE standard luminosity function. $\bar{y}(\lambda)$, plotted in Figure 2-3, approximates the sensitivity of the human eye to various wavelengths.

Luminance, L_v , often called “brightness,” quantifies luminous flux perceived by a human eye from a certain angle and is measured in candelas (Cd) per square meter. It is calculated as

$$L_v = \frac{\Phi_v}{2\pi \times A_{LED}} = \frac{683}{2\pi} \times \frac{\int_{380}^{780} \frac{G \times I_{pc}}{R_{pd}(\lambda)} \bar{y}(\lambda) S(\lambda) d\lambda}{A_{LED} \times \int_{380}^{780} S(\lambda) d\lambda} [Cd/m^2] \quad (2.9)$$

An alternative efficiency metric for devices emitting in the visible regime is power efficiency ([lm/W]), F_w , which accounts for the sensitivity of the human eye to various wavelengths. This is calculated as the ratio of the luminous flux to the power input into the device:

$$F_w = \frac{\Phi_v}{IV} = \frac{2\pi L_v}{IV} \times 100\% \quad (2.10)$$

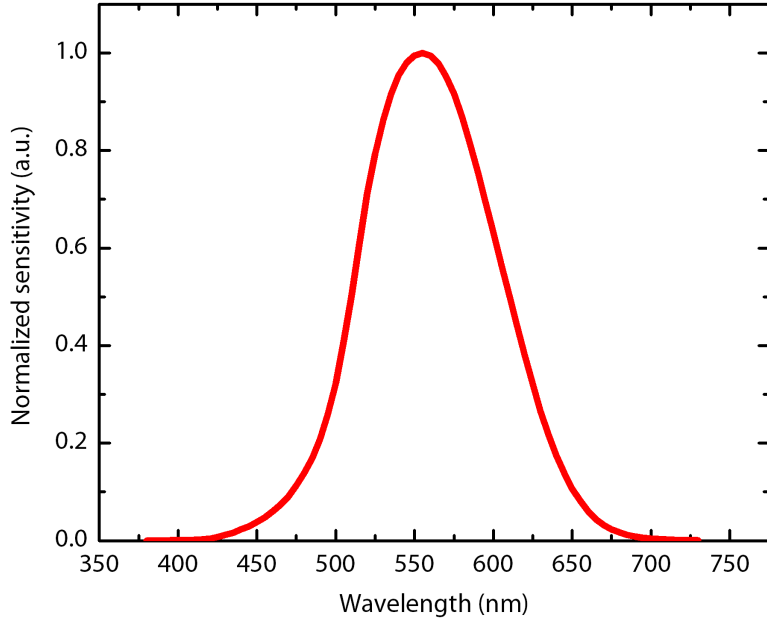


Figure 2-3: 1924 CIE standard luminosity function.

The human eye has virtually zero sensitivity to light in the infrared regime, so for infrared devices, “peak radiance,” $R([\frac{W}{m^2sr}])$, is a more reasonable metric of brightness than luminance. This is defined as the light output power collected by the photodetector normalized by the device area and the number of steradians captured by the photodetector:

$$R = \frac{L}{A_{LED} \times \frac{A_{pd}}{d^2}} [\frac{W}{m^2sr}] \quad (2.11)$$

where A_{LED} is the area of the devices, A_{pd} is the active area of the photodetector, and d^2 is the distance from the front of the device to the photodetector.

Chapter 3

Electrophoretic Deposition of CdSe/ZnS Quantum Dots

3.1 Motivation

The most efficient QD-LEDs to date are fabricated with thin QD films that are deposited by spin casting colloidal QD solutions [32, 33]. Spin casting is a straightforward process that yields films of controllable and uniform thickness, but it is somewhat unscalable, as the parallel processing of multiple substrates would require multiple spinners. In addition, spin casting does not efficiently utilize materials, as a large proportion of solution used in spin casting is spun off the substrate and is unrecoverable.

Several alternatives to spin casting have been explored in recent years. For example, contact printing, whereby QDs are spun onto an elastomer stamp and subsequently transferred onto the substrate of interest, has been used to fabricate QD-LEDs with feature sizes on the order of $25 \mu\text{m}$ [19]. This feature, along with ability to have multiple pixel colors on the same substrate, makes this technique especially promising for high resolution, full color displays. Ink jet printing is another technique that can be used to produce patterned QD films, with the advantages of high material utilization and processing simplicity but the drawbacks of lower pattern resolution and less film thickness and roughness uniformity [18, 34].

Electrophoretic deposition (EPD), the subject of this chapter, is a technique that has been used to deposit a variety of materials, including quantum dots and other nanoscale particles, on conducting substrates [35, 36]. In EPD, an applied electric field between two electrodes submerged in a solution drives the deposition of particles in the solution onto the electrodes. EPD is a highly scalable process: multiple substrates may be prepared in the same EPD bath, and as is the case in ink jet printing, all of the starting materials may be salvaged in EPD. It is highly conformable, allowing for deposition onto electrodes of arbitrary shape, size, and texture. In addition, unlike spin casting, which is a rapid process that forms disordered films in which particles may not be in a mechanical equilibrium, EPD is a slower deposition process that may allow particles to assemble in a more energetically favorable manner on the surface of the substrate. Several reports have been made on the EPD of QD films [37, 38], one of which even demonstrates that EPD of CdSe QDs can produce patterned films with feature sizes on order of 10-20 nm when a diblock copolymer template is used to control QD placement [39]. The EPD of QD films has further been demonstrated to yield QD photovoltaics of respectable performance [40, 41, 42].

Unfortunately, all electrophoretically deposited QD films reported to date are too thick and resistive to be used in the most modern QD-LED architecture, which requires that the QD layer be only a few monolayers in thickness for efficient electroluminescence. Furthermore, these reports have focused on the deposition of core-only QDs composed of a single compound, such as CdS. As mentioned previously, however, the most efficient QD-LEDs to date have utilized core-shell QDs, in which the QD core is overcoated by a wide bandgap shell (e.g. ZnS), increasing the photoluminescence quantum yield (PL QY), protecting the emissive core from PL quenching processes, and boosting the photo-oxidative stability of the dots, all features that are highly beneficial for QD-LEDs [26]. This chapter discusses the development of an EPD technique to produce thin CdSe/ZnS QD films for use in QD-LEDs.

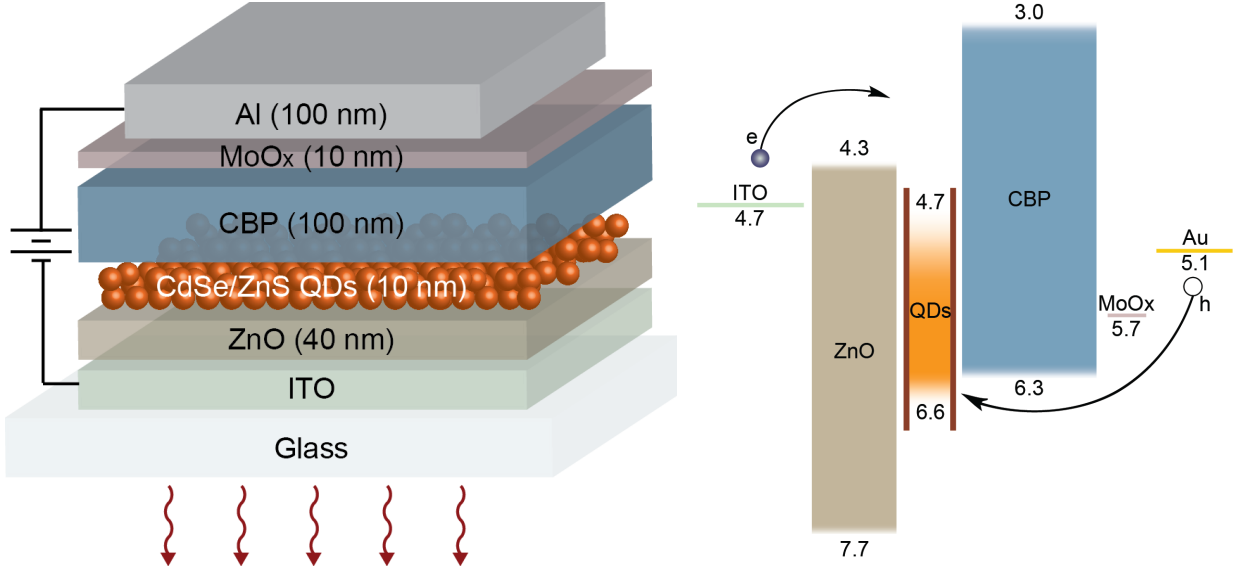


Figure 3-1: Schematic cross section of the QD-LED structure used for EPD and control devices (left) and the corresponding flat-band energy diagram (right) with energy levels taken from literature [2, 3, 4, 5, 6].

3.2 Methods

3.2.1 Fabrication of QD-LEDs

Fabrication of the QD-LEDs starts with a commercially purchased, pre-patterned indium tin oxide (ITO) electrode on a glass substrate. After the substrate is washed with solvents and cleaned with oxygen plasma exposure (procedure detailed in Appendix A), a ~ 40 nm thick zinc oxide (ZnO) electron transport layer is formed by spin-casting zinc acetate [Zn(ac)] solution onto the substrate and annealing it at 300°C for 5 minutes in air. Next, a $\sim 10\text{-}15$ nm thick QD film is electrophoretically deposited in the EPD process described in the next section in detail. The samples are then transferred into a vacuum chamber (with a base pressure of 10^{-6} Torr), where a 100 nm thick 4,4'-N,N'-dicarbazolebiphenyl (CBP) hole transporting layer, a 10 nm thick molybdenum oxide (MoO_x) hole injection layer, and a 100 nm thick aluminum (Al) anode are deposited by sequential thermal evaporation. The completed device, along with the corresponding flat band energy diagram, is shown in Figure 3-1, where energy levels are taken from literature [2, 3, 4, 5, 6].

QDs used here are CdSe/ZnS core-shell dots provided by QD Vision Incorporated. They are capped with carboxylic acid ligands, roughly estimated to be 5 carbons long from ligand exchange experiments not described in this thesis. The photoluminescence (PL) peak of the QD solution used in this study appears at a wavelength of 610 nm (red-orange), and each QD-ligand complex is 8-10 nm in diameter. They are received in hexane and are crashed out in air twice and redissolved in chloroform in ONE Lab (see Appendix A for detailed procedure). For control devices, a QD solution calibrated for a known end thickness is spun onto the ZnO-on-ITO/glass stack in a nitrogen ambient glovebox.

3.2.2 Electrophoretic deposition procedure

Successful EPD of thin QD films for the QD-LEDs with an EPD layer (referred to from here as the “EPD devices”) is conducted via a 2-step process that is shown schematically in Figure 3-2. First, two vials are prepared – for the first step, a few milliliters of a 0.1 mg/mL QD solution in a mixture of chloroform and acetonitrile (10:1 ratio) is poured into a 20 mL amber vial, and for the second step, another amber vial is filled with neat chloroform. An amber vial is used to minimize exposure of the QDs to light, which may influence the dynamics of the deposition, as discussed in Section 3.4. The two prepared vials are then capped to prevent evaporation and placed into a sonication bath in air.

A custom-machined polytetrafluoroethylene (PTFE or Teflon) sample holder parallelly secures two 0.5” × 0.5” ZnO-on-ITO electrodes 0.4 cm apart with their conductive sides facing each other. The strength of the carbon-fluorine bonds in Teflon grants it resistance to chloroform, the main solvent used here. The sample holder suspends the electrodes in the deposition vials in a reproducible way and allows a power supply to be connected in order to establish a voltage bias between the electrodes. To prepare for deposition, a power supply is connected to the sample holder, and a voltage is applied between two secured electrodes. The sample holder with the two electrodes in place is then placed into the vial containing the QD solution in the sonication bath, and deposition proceeds for a few minutes. After a specified

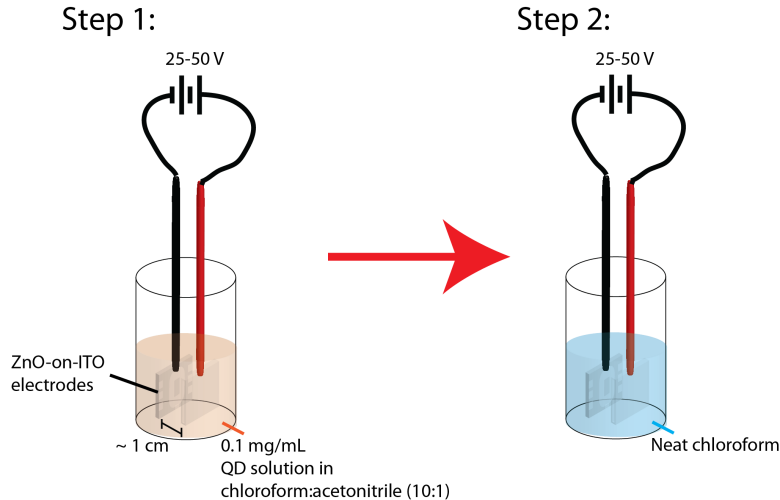


Figure 3-2: Schematic of a 2-step electrophoretic deposition process for the formation of thin, luminescent QD films.

amount of time, the sample holder is lifted out of the first vial and, with the voltage bias remaining on, is placed into the second vial that is filled with chloroform for 15 seconds. This rinsing step removes aggregates and QDs that are not well-bound to the surface of the electrodes, as well as QD-rich solvent droplets that leave behind uneven QD deposits upon drying.

The addition of acetonitrile to the first deposition vial plays a critical role in enabling the deposition of QDs. Figure 3-3 plots current through the EPD setup under an applied bias of 50 V/cm and demonstrates a shape consistent with electrophoretic deposition. As noted in Figure 3-3, the current through the deposition setup when no acetonitrile is present is 1-2 orders of magnitude lower than that when acetonitrile is present. This is not surprising because acetonitrile decreases the solubility of QDs in solution, possibly by partially removing ligands that solubilize the QDs. This exposes charge traps on the surface of the QDs, making the QDs more affected by the external electric field and thus increasing the rate of deposition. On the other hand, an excess of acetonitrile and/or other similar solvents, such as acetone, causes QDs to visibly crash out of solution, leading to thick films composed of large QD agglomerates.

After the EPD of the QD film is complete, the samples are transferred to a nitrogen ambient glovebox and remain in an oxygen-free environment for the remainder of the

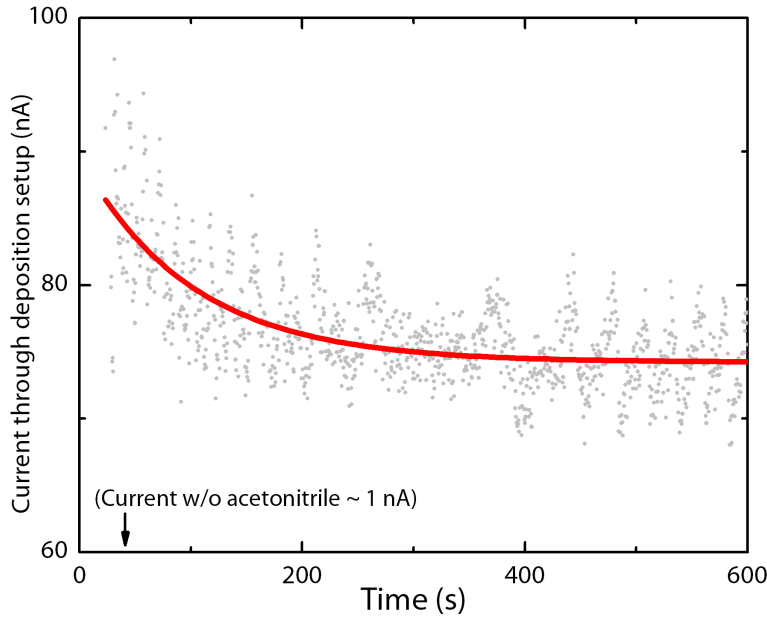


Figure 3-3: Current through EPD setup versus time.

fabrication process, which is described in the previous section and in Appendix A.

3.3 Film characterization

3.3.1 Roughness and thickness

Both the roughness and the thickness of a QD are important in fabricating an efficient QD-LED. Films must be smooth to allow subsequent layers to be deposited as flat films without shorting pathways, and in the hybrid inorganic-QD-organic structure used here, they must be thin to allow for efficient charge transport and electroluminescence. Tapping-mode atomic force microscopy (AFM) is used to characterize the thickness and roughness of the films. In tapping-mode AFM, a Si cantilever with a tip that has a radius of curvature of ~ 10 nm oscillates near its resonant frequency. Interactions between the surface of a sample and the cantilever tip cause variations in the amplitude and frequency of the cantilever oscillations. The tip scans a two-dimensional area of the sample, maintaining a distance from the surface that allows cantilever-surface interactions to be detected without physical contact to the sam-

ple, which could cause the tip to stick and/or drag particles along the surface of the sample. Analysis of the resulting topography/height and phase images allows for the resolution of nanometer-scale features and extraction of important morphological metrics, such as roughness.

Figure 3-4 shows an AFM topography image of a $2\mu\text{m} \times 2\mu\text{m}$ area of QDs electrophoretically deposited onto a ZnO-on-ITO substrate. EPD lasted for 5 minutes under a 20 V applied bias (electric field of 50 V/cm), and the film shown was deposited on the anode (+). Analysis with WSxM software indicates a root-mean-square (RMS) roughness of 2.3 nm [43]. The RMS roughness of the underlying ZnO-on-ITO is \sim 1.5 nm, indicating that the low roughness of the EPD QD film is not simply a result of filling in large voids on a rough electrode. With QDs 8-10 nm in diameter, a 2.3 nm RMS roughness translates to a mere fraction of a QD monolayer.

AFM is also used to evaluate the thickness of a thin QD film. A film can be simply scratched with a razor blade, and a one-dimensional AFM scan is run to measure the step height. Figure 3-5 plots an 85-nm-long AFM line scan across a razor blade scratch in an EPD QD film (deposited using the same conditions of the EPD film shown in Figure 3-4) and indicates that the thickness of the film is 15 nm. The thickness can

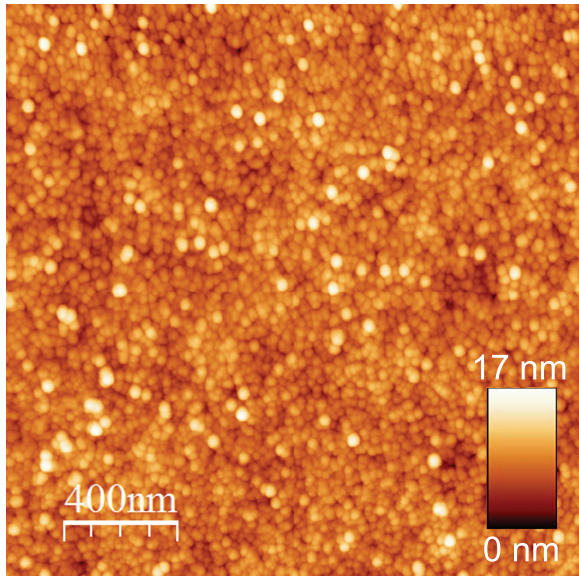


Figure 3-4: AFM topography image of EPD QDs on a ZnO-on-ITO anode. EPD lasted for 5 minutes under a 20 V applied bias (electric field of 50 V/cm).

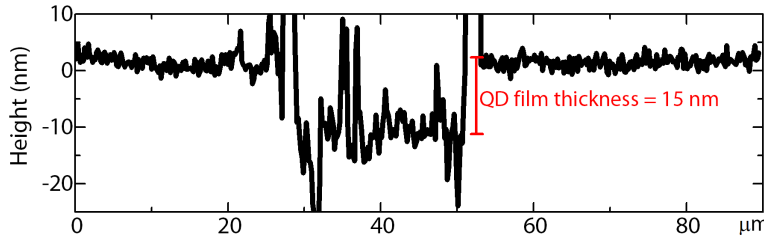


Figure 3-5: Step profile of scratch in an anodic EPD QD film (5 minute deposition under a field of 50 V/cm) showing a film thickness of 15 nm.

ideally be varied by adjusting the concentration of QDs in the solution used, voltage used to drive EPD, degree of acetonitrile added, and length of deposition.

3.3.2 Photoluminescence of anode versus cathode

Figure 3-6 shows photographs of FTO electrodes after EPD under ambient light (left) and their photoluminescence in the dark under a UV lamp (right). EPD of the films shown in this figure was done in a clear quartz cuvette in a dark, covered box, and the deposition was carried out for 25 minutes under an electric field of 50 V/cm. Acetone was added to the chloroform:acetonitrile solvent mixture (chloroform:acetone:acetonitrile = 11:3:1). The deposition directly onto a conductive electrode, longer deposition time, and harder crash-out resulted in the deposition of the very thick (>100 nm) films shown in Figure 3-6. The films used for devices were visibly thinner than those shown in the photographs, but like those shown in the photographs, there was consistently a preferential deposition of luminescent dots onto the anode, though to a less obvious extent.

This difference in photoluminescence between the anode and cathode was more pronounced when EPD was carried out in a clear vial instead of an amber one, suggesting that light exposure could play a role in charging or inducing dipoles in QDs in solution or otherwise changing the dynamics of the deposition. It is unclear if the difference in photoluminescence originates from a difference in film thickness, packing density, and/or an inherent optical difference between positively-charged and negatively-charged QDs.

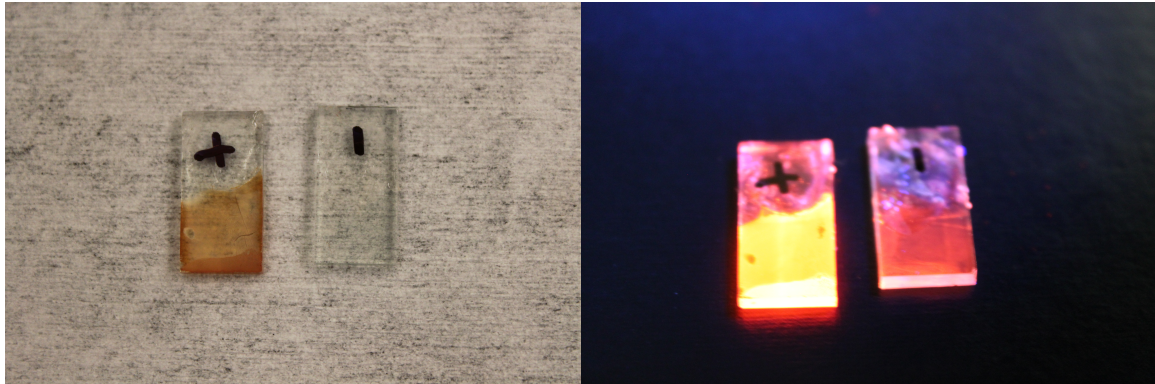


Figure 3-6: Photographs of anode (+) and cathode (-) of EPD QD films on FTO electrodes under ambient light (left) and in the dark under a UV lamp (right) demonstrating that a more photoluminescent film forms on the cathode.

3.4 Optically patterning films

This section describes preliminary experiments that suggest that it may be possible to guide patterned EPD of QDs with laser light. During the experiment used to create the films seen in Figure 3-6, a ~ 50 mW, 532 nm (green) laser was positioned to hit a single spot on each of the electrodes. As seen in Figure 3-7, a dark spot was left behind on the anodic film where the laser shone.

Elemental analysis can be done via energy-dispersive X-ray spectroscopy (EDX). A scanning electron microscope (SEM) is fitted with an energy-dispersive spectrometer. X-rays characteristic of a certain atom are emitted and subsequently detected by this spectrometer when an incident electron beam from the SEM strikes an atom and excites an electron to a higher energy level. Figure 3-7 shows the EDX map of the edge of the dark spot. The decreased presence of Zn and S, the elements comprising the QD shell, inside the spot and increased presence of Sn, an element in the underlying FTO electrode, inside the spot suggest that the laser may have played a role in preventing the deposition of dots.

To further investigate this effect, the experiment was repeated with the laser shining through a single slit, creating a diffraction pattern and effectively forming a line on the electrodes during EPD. The result is shown in Figure 3-8, a photograph of photoluminescence from an EPD cathode under a UV lamp. The slightly darkened

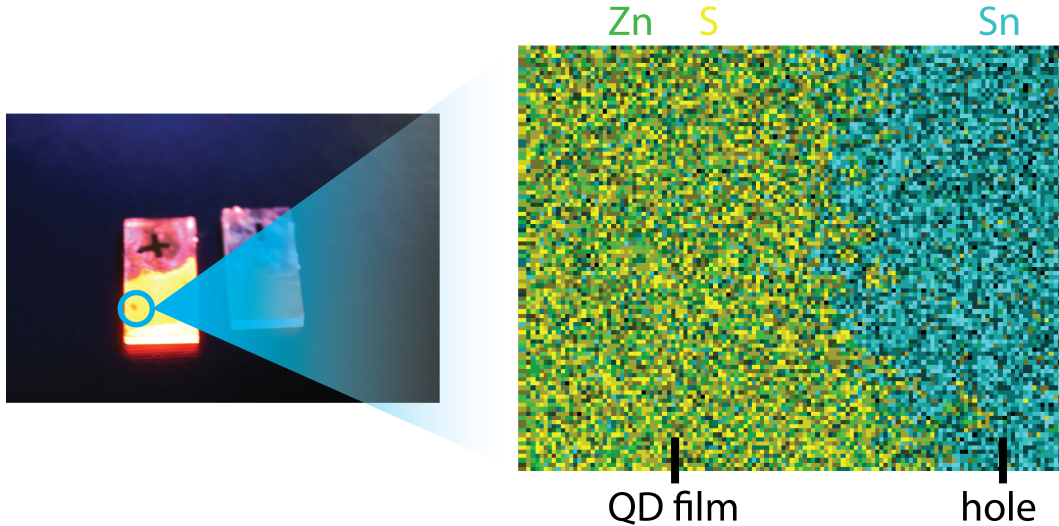


Figure 3-7: Energy dispersive X-ray spectroscopy map of the edge of the dark spot on the cathode shown in Figure 3-6. Green pixels mark the presence of Zn, yellow pixels mark the presence of S, and teal pixels mark the presence of Sn (from the underlying FTO).

line seen in the photograph appeared where the laser shone. Similarly, in an experiment in which the laser line was tilted, a diagonal line appeared on the cathode. However, EDX elemental analysis and AFM surface analysis reveals that, in contrast to the previous result, there is no notable decrease in the presence of QDs in these lines, suggesting that perhaps the laser merely photobleaches (decreases the photoluminescence of) the dots in the areas it shone onto.

More studies must be done to understand, confirm, and manipulate this phenomenon before it can be used in a practical way for patterning. In the follow up experiments that were conducted, darkened areas where a laser was shone did not appear consistently, and the electrode (anode vs. cathode) that showed this effect varied from experiment to experiment.

3.5 Device performance

Figure 3-9 shows 10 simultaneously lit EPD QD-LEDs operating at approximately 100 cd/m^2 (a brightness level often taken to be “video brightness”). The devices show pure QD emission, confirmed by electroluminescence (EL) spectra in Figure 3-13. For

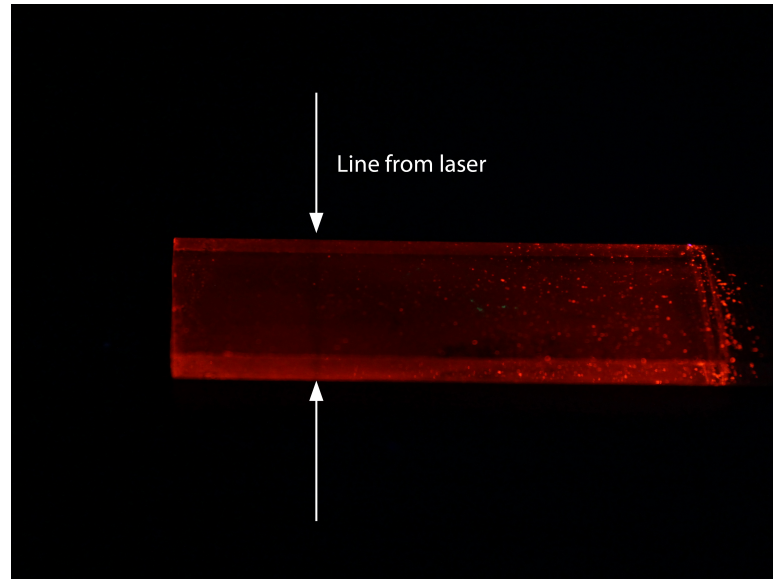


Figure 3-8: Photograph of EPD cathode photoluminescence under a UV lamp. The position of the darkened line (marked by an arrow) is in agreement with the placement of a line of green laser light shone onto the substrate during EPD.

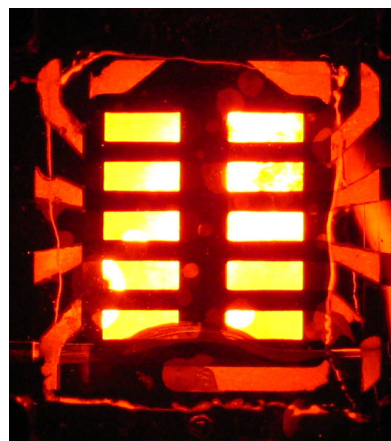


Figure 3-9: 10 simultaneously lit devices operating at approximately 100 cd/m^2 .

further evaluation, control devices with a 10 nm spun-cast QD layer and EPD devices with QD films electrophoretically deposited under various conditions were tested and evaluated using methods described in Chapter 2.

Figure 3-10 shows current density versus voltage curves for QD-LEDs with an EPD QD layer and a spun-cast QD layer. The EPD device shown served as the anode (positive electrode) during EPD, and deposition was conducted for 5 minutes under a field of 25 V/cm. The QD film was found to be approximately 15 nm thick. The $J - V$ curves show an expected transition from ohmic conduction at voltages below the optical turn-on of the device (where $J \propto V$) to trap-limited conduction ($J \propto V^{n+1}, n \geq 1$) at voltages above the optical turn-on.

Figure 3-11 plots current through a Si photodetector against voltage applied to the QD-LEDs described above. The turn-on voltage is estimated from these curves as the voltage needed to induce a photocurrent of 0.1 nA, a value above the noise level of the photodetector and one corresponding to a brightness level on the order of 0.1 Cd/m². From this figure, the turn-on voltages are estimated as 1.9 V for the EPD device and 2.1 V for the control device. In general, a lower QD film thickness often

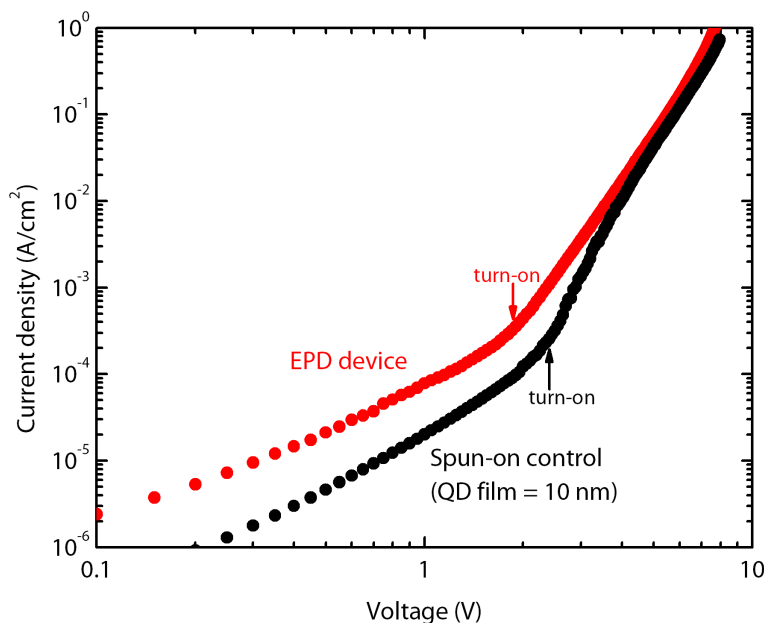


Figure 3-10: Current density versus voltage for QD-LEDs with an EPD QD layer (red) and a spun-cast QD layer (black).

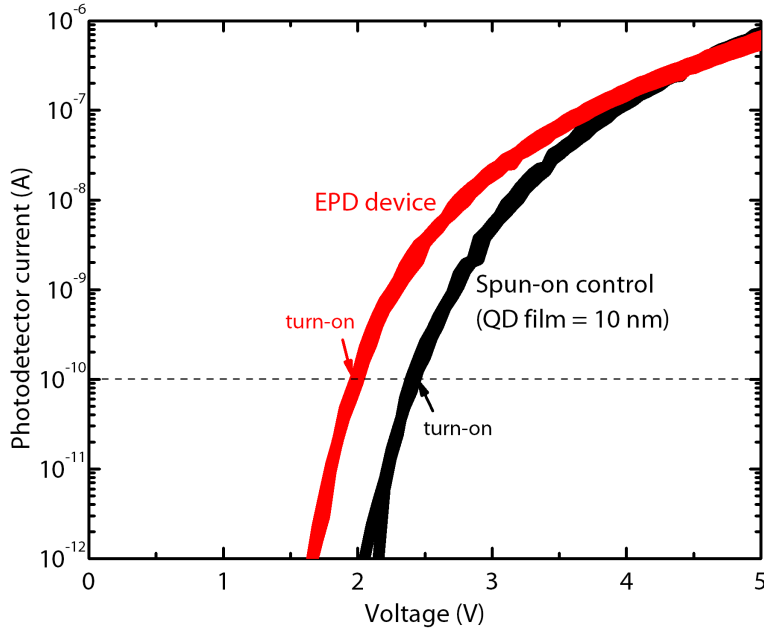


Figure 3-11: Photodetector current versus voltage for QD-LEDs with an EPD QD layer (red) and a spun-cast QD layer (black).

correlates with a lower turn-on voltage, and because the film thickness of the EPD QD layer was measured via AFM to be in fact slightly thicker than the calibrated thickness of the spun-cast QD layer, a difference between the film thickness of the EPD QD layer and the spun-cast QD layer is unlikely to explain the observed decrease in turn-on voltage in the EPD device. In fact, given the ~ 2 V optical band-gap of the QDs, the 1.9 V turn-on for the EPD devices is surprisingly low, and the mechanism of this is not understood.

Figure 3-12 plots external quantum efficiency (EQE) versus current density for control QD-LEDs with a 10 nm spun-cast QD layer; QD-LEDs with a “dipped” QD layer, in which a ZnO-on-ITO electrode underwent the EPD process described previously with a 0 V EPD bias; and QD-LEDs with QD layers electrophoretically deposited under different conditions. In one deposition, 10 V was applied for 5 minutes between 2 ZnO-on-ITO electrodes, and in a second deposition, 20 V was applied for 1 minute between 2 ZnO-on-ITO electrodes. The anodes and cathodes from both these depositions were subsequently made into completed QD-LEDs. As seen in Figure 3-12, the peak EQE of the highest performing EPD device – the anode from the 10

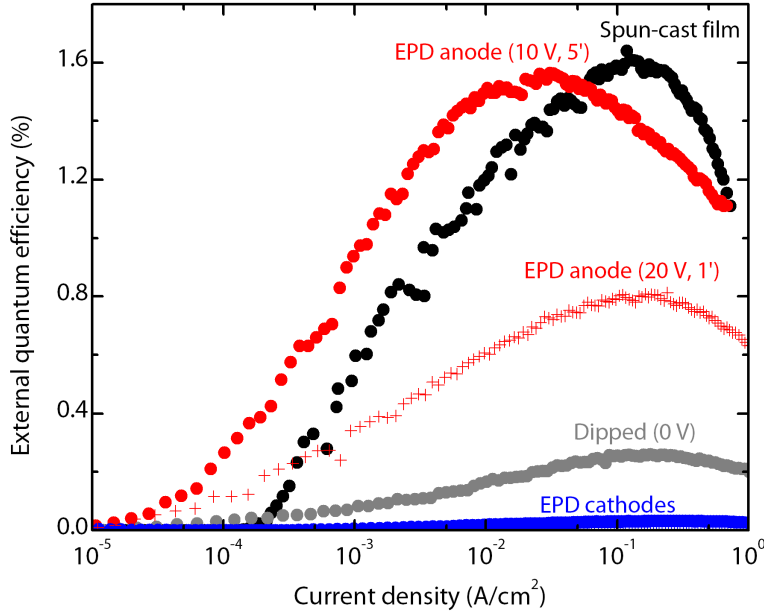


Figure 3-12: External quantum efficiency versus current density for QD-LEDs with a spun-cast QD layer, a dip-coated QD layer, and various EPD QD layers.

V (field of 25 V/cm), 5 minute deposition – is 1.5%, which is comparable to the 1.6% peak EQE of the control device. The EPD anode device from the 20 V (field of 50 V/cm), 1 minute deposition also shows a respectable EQE of 0.8%. The dipped device achieve an EQE of approximately 0.3%, and both EPD cathode devices peak at EQEs less than 0.1%. The improved EQEs of EPD anode devices over those of dipped and cathode devices was a repeatable phenomenon, but the exact conditions that led to the EPD device with the highest EQE varied from experiment to experiment. A study by M. Islam *et al.* showed that the presence of impurities, including free ligands, in the solution used to form electrophoretically deposited, 0.5- μm -thick CdSe nanocrystal films greatly affects nanocrystal aggregation and adhesion to the electrode [38]. A similar impurity-induced variation in film morphology and thickness is very likely present in our setup and would indeed in turn cause a variation in QD-LED performance, explaining the variation in optimal EPD parameters between runs.

Figure 3-13 shows the electroluminescence (EL) spectra of the control QD-LED and the EPD anode and cathode devices from the 10 V, 5 minute deposition. EL spectra are collected using a calibrated Ocean Optics spectrometer placed over a device operating at approximately 100 Cd/m². The observed red shift and spectral

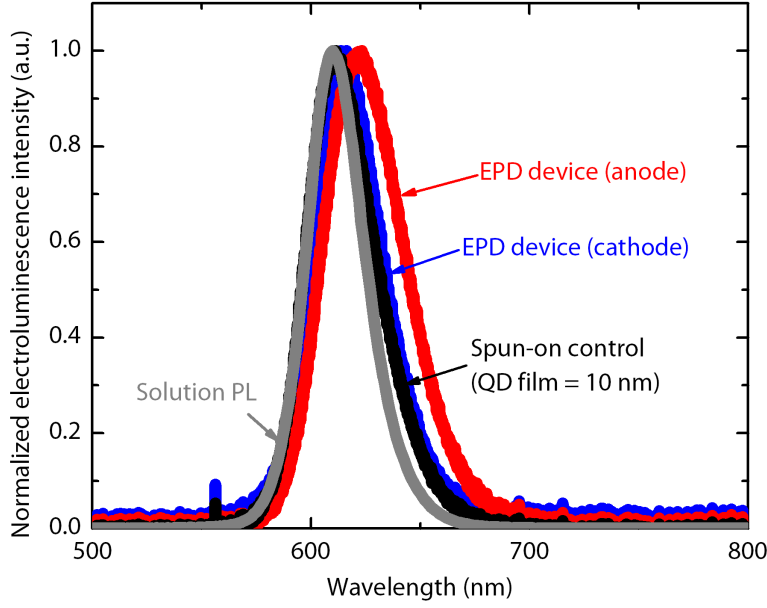


Figure 3-13: Electroluminescence spectra for QD-LEDs operating at $\sim 100 \text{ Cd/m}^2$. The photoluminescence spectrum of the starting QD solution is provided for reference.

broadening between the solution PL and QD-LED EL spectra comes from a combination of an electric-field-induced Stark effect and a red shift in PL spectra of the QDs from solution to thin-film, a state in which the wavefunction overlap between QDs is increased, leading to exciton delocalization.

Table 3.1: Electroluminescence peak and width of control and EPD QD-LEDs

	Spin-casting	Dipped	EPD cathode	EPD anode
Peak λ	611 nm	616 nm	616 nm	623 nm
FWHM	38 nm	42 nm	38 nm	45 nm

Table 3.1 lists the peak wavelength and full-width-half-maximum (FWHM) of the EL spectra of the control, EPD anode (from the 10 V, 5 minute deposition), EPD cathode (from the 10 V, 5 minute deposition), and dipped QD-LEDs. EPD anode devices consistently show a greater red shift and a broader EL spectrum than EPD anode devices, which show only a small red shift and degree of broadening compared to control devices with a spun-cast QD layer. Figure 3-14 shows the EL peak of EPD devices produced under various deposition conditions. There appears to be a possible upward trend in peak wavelength in EPD cathode devices with

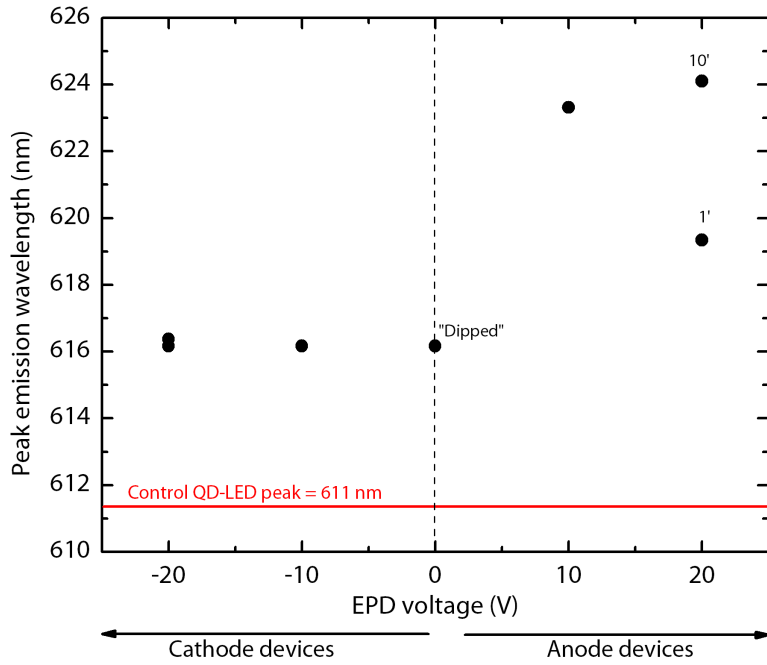


Figure 3-14: Electroluminescence peak wavelengths for EPD QD-LEDs with different EPD conditions. The red line indicates the peak wavelength of control QD-LEDs (with a 10 nm spun-cast QD layer). EPD anode devices lie in the positive voltage half of the plot (right), and the EPD cathode devices lie in the negative voltage half of the plot (left).

increasing EPD voltage and no trend in EPD anode devices with increasing EPD voltage. However, more data points are needed to confirm this.

This red-shift can be attributed to a denser QD film, which would exhibit a solvatochromic red-shift [44]. Alternatively, the red-shifted emission might originate from QD agglomerates that could form in the presence of acetonitrile even before their deposition onto the electrodes [45]. Finally, it is possible that the anodic EPD process forms a permanent electric dipole layer at the interface with the ZnO film, which would affect the QDs via the electric-field-induced Stark shift.

3.6 Summary

This chapter presents a new electrophoretic deposition technique for producing thin, bright films of QDs for use in QD-LEDs. 10-15 nm-thick QD films with an RMS roughness of 2 nm could be produced with this 2-step EPD process. The best EPD

devices, made from an EPD anode, show EQEs of 1.5% – comparable to that of control QD-LEDs made with a spun-cast QD layer. It is expected that this technique can be readily extended to deposit dots of a different size and/or material, including near-infrared PbS/CdS QDs. There are many more experiments, not addressed in this thesis, that should be done to better understand and control the phenomenon described here, including the discrepancy between EPD anode and EPD cathode devices and the possible optical patterning of films.

Chapter 4

Near-Infrared QD-LEDs

4.1 Motivation

Near-infrared (NIR) light sources with emission wavelengths $\lambda > 1 \mu\text{m}$ have found widespread use in many applications, such as optical telecommunications [46] and biomedical imaging [47]. As mentioned in the introduction, current NIR light sources are conventionally made from crystalline inorganic semiconductors, which are often grown via high-temperature, costly processes. Unfortunately, while organic light-emitting devices (OLEDs) offer low-cost alternatives in the visible regime, the photoluminescence quantum yield (PL QY) of organic dyes in the NIR are severely limited [48]. On the other hand, QD-LEDs, which possess many of the same desirable characteristics of OLEDs, do not suffer from such a limitation. The PL of QDs can easily be tuned, with high solution PL QY maintained throughout both the visible (QY $> 95\%$ [49]) and NIR (QY $> 40\%$ [26]), making them an attractive option for economical NIR light emitters. NIR QD-LEDs with peak EQEs of 2% – nearly 10 times those of NIR OLEDs – have been demonstrated [50, 48], but the highest performance NIR QD-LEDs reported to date still lag behind their visible QD-LED counterparts, which exhibit peak EQEs up to 7% in the red [51]. One possible reason for this is that whereas visible QD-LEDs utilize core-shell QDs, NIR QD-LEDs reported in literature largely rely on core-only QDs. As mentioned in the introduction, a wide band-gap shell helps screen QDs from external PL quenching and increases photo-oxidative sta-

bility [26]. Furthermore, whereas the most efficient visible QD-LEDs take advantage of the inorganic-QD-organic hybrid structure introduced in previous chapters, NIR QD-LEDs to date rely on more primitive structures that place QDs next to conductive, quenching materials. The work presented in this chapter presents NIR QD-LEDs that rely on core-shell PbS/CdS QDs and are fabricated in a hybrid QD-LED structure. The use of core-shell PbS/CdS QDs results in a nearly 100-fold enhancement of peak EQEs over PbS core-only controls. Wall-plug efficiencies and radiances of these core-shell devices are also greater than those of previously reported NIR-emitting QD-LEDs, making this work a demonstration of the highest-performance NIR QD-LED to date [50].

4.2 Methods

4.2.1 Synthesis of core-shell PbS/CdS NIR QDs

QDs used in this study are synthesized by Gyuweon Hwang in the Bawendi Lab using the method reported by S. Geyer *et al.* [24]. First, a lead precursor is prepared by heating 30 mmol of lead acetate trihydrate (Sigma Aldrich), 125 mL of octadecene (Sigma Aldrich), and 175 mL of oleic acid (TCI) in a round-bottomed flask for 12 hours under vacuum at 100°C. A sulfur precursor is prepared by adding 15 mmol hexamethyldisilathiane (Fluka) to 150 mL of octadecene. The lead precursor is placed under flowing nitrogen and heated to 150°C before injection of the sulfur precursor. This solution is then cooled to room temperature and transferred into a nitrogen-filled glove box without air exposure. The QDs are purified by adding methanol and 1-butanol until the solution is turbid. Centrifugation is subsequently used to precipitate the QDs. The supernatant is discarded, and the QDs are re-dissolved in hexane. This crash-out process is repeated two more times, and after the final crash-out, the QDs are re-dissolved at 40 mg/mL in chloroform. The resulting oleic-acid-capped PbS QDs are on average 4.0 nm in diameter with a peak solution PL wavelength of 1315 nm.

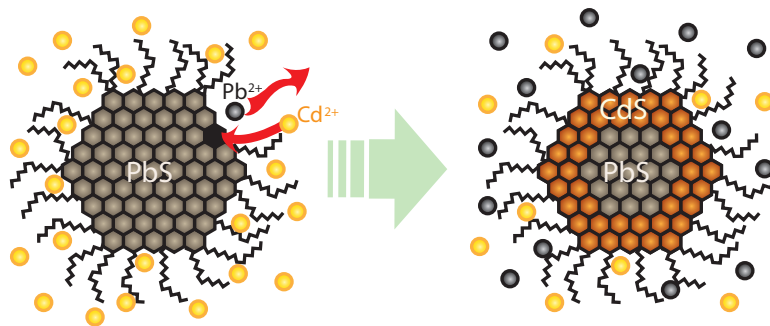


Figure 4-1: Schematic of a cation exchange process for the growth of a CdS shell on PbS QDs.

CdS shells are formed around the PbS QDs by cation exchange, a process represented schematically in Figure 4-1 [26, 52]. For lead chalcogenide QDs, conventional shell growth techniques like those described in the introduction are complicated by the tendency of cadmium chalcogenide and other shell precursors to nucleate as homogeneous nanocrystals instead of grow as shells onto the lead chalcogenide QDs [26]. Cation exchange is a reaction that avoids this problem while also taking advantage of the fact that Pb^{2+} ions near the surface of Pb chalcogenide QDs are prone to replacement by other metal ions in excess in solution [26]. Cadmium oleate, a relatively slow-reacting precursor, is selected as the precursor for CdS shell growth here to allow for more control over shell thickness than faster-reacting precursors that could result in a total replacement of Pb^{2+} by Cd^{2+} . An excess of cadmium oleate is added to the core-only PbS QD solution under flowing nitrogen to drive the replacement of Pb^{2+} by Cd^{2+} , resulting in the inward growth of a CdS shell into the PbS QDs. The solution is held at 80 to 100°C for between 5 minutes and 2 hours, depending on the desired shell thickness. For this study, PbS/CdS QDs with shell thicknesses ranging between 0.18 nm to 0.69 nm (with QD core sizes of 3.64 nm and 2.62 nm,

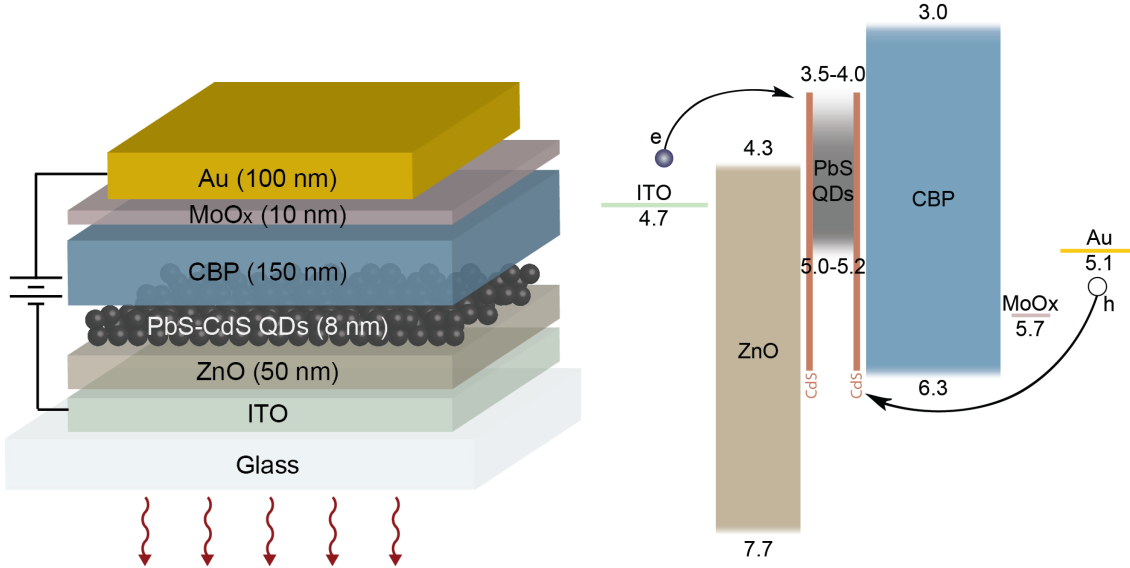


Figure 4-2: Cross-section schematic of NIR QD-LEDs and the corresponding flat-band energy diagram, with energy levels taken from literature [2, 3, 4, 5, 6].

respectively) were prepared. All QD solutions are filtered with a $0.45\ \mu\text{m}$ PTFE mesh immediately before use.

4.2.2 Fabrication of NIR QD-LEDs

Figure 4-2 shows the cross section schematic and corresponding flat band energy diagram for NIR QD-LEDs, with energy levels taken from literature [2, 3, 4, 53, 5, 6]. These NIR QD-LEDs are fabricated using the method described previously for the fabrication of the spun-cast control QD-LED in Chapter 3. For the NIR devices here, however, 150 nm CBP is used instead of 100 nm. As will be discussed in Chapter 5, increasing the thickness of CBP plays a key role in optimizing the peak efficiency of these devices. In addition, a 100 nm Au anode is thermally evaporated in place of the 100 nm Al anode used previously. This replacement is not seen to have a noticeable effect on device performance.

QD film thickness must be carefully calibrated and controlled for each QD solution in order to make accurate comparisons among devices made with different solutions. To calibrate a solution, films are spun-cast onto ZnO (prepared identically to the ZnO in completed QD-LEDs) from several different dilutions of the QD solution. An area

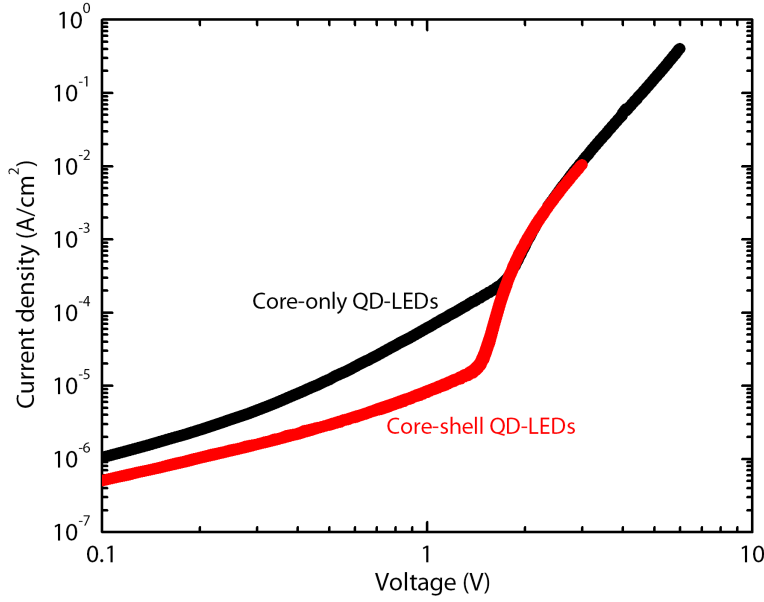


Figure 4-3: Current density vs. voltage curves for QD-LEDs made with core-shell PbS/CdS (shell thickness = 0.21 nm) QDs (red) and with core-only PbS QDs (black).

of the spun-cast QD film is gently wiped off with chloroform using a polyurethane swab (VWR), and the resulting step is measured using a profilometer (Tencor P16). Each sample is measured 3-5 times, and the film thickness corresponding to that particular solution dilution is taken to be an average of these measurements (wiping a plain ZnO film without a QD film results in no detectable step). A linear fit of the QD film thickness versus QD solution concentration data yields the solution concentration necessary to form the 8 ± 1 nm films used in all QD-LEDs. For a spin speed of 1500 rpm, approximately 5 mg/mL of QD solution is needed to form such films.

4.3 Efficiency and brightness of PbS/CdS QD-LEDs

Figure 4-3 shows representative current density vs. voltage curves for QD-LEDs made with core-shell PbS/CdS QDs (shell thickness = 0.21 nm) and for QD-LEDs made with core-only PbS QDs. The core-shell QD-LEDs show a lower off-current than the core-only control devices, and they transition from an ohmic conduction regime ($J \propto V$) to a trap-limited one ($J \propto V^{n+1}$ for $n > 1$), at a lower turn-on voltage.

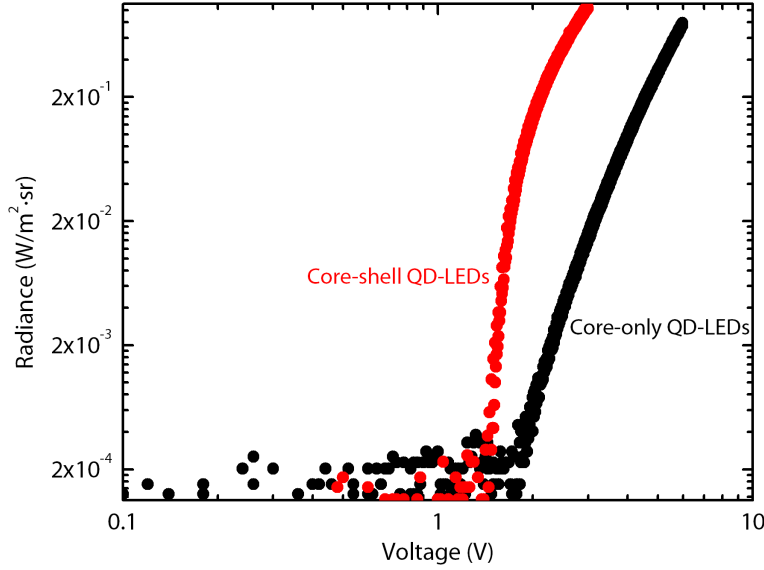


Figure 4-4: Radiance vs. voltage curves for QD-LEDs made with core-shell PbS/CdS (shell thickness = 0.21 nm) QDs (red) and with core-only PbS QDs (black).

This is corroborated by the radiance vs. voltage curves plotted in Figure 4-4. A calibrated germanium photodetector is placed over the device during testing to collect light, and radiance is calculated as detailed in Chapter 2. This data shows that the addition of a shell results in a reduction in turn-on voltage, measured at 3×10^{-4} W/(m²· sr), from 2.0 V to 1.4 V. This reduction suggests that charge injection into the QDs is more efficient when the PbS QDs are overcoated with a CdS shell.

EQE, calculated as described in Chapter 2, is plotted in Figure 4-5. The EL spectrum (not shown) reveals pure QD emission without noticeable emission features from the ZnO and CBP charge transport layers. For simplicity, here, EQE is estimated by assuming the EL spectrum of the device to be a Kronecker delta function centered at the peak PL wavelength; more rigorous calculations that account for the spread in the actual EL spectrum confirm that the numbers presented here are indeed representative. The peak EQE for the core-shell QD-LEDs shown is 4.4% – a nearly 100-fold improvement over the 0.05% peak EQE of the core-only QD-LEDs. From the light output power and current-voltage data, average power (“wall-plug”) efficiency,

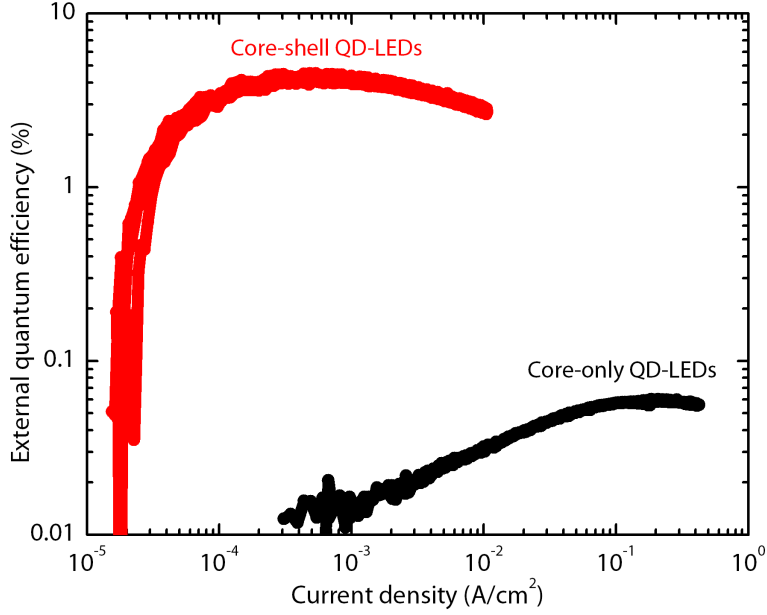


Figure 4-5: External quantum efficiency vs. current density curves for QD-LEDs made with core-shell PbS/CdS (shell thickness = 0.21 nm) QDs (red) and with core-only PbS QDs (black).

another often-cited performance metric, can be calculated as:

$$E = \frac{L}{IV} \times 100\% \quad (4.1)$$

The core-shell devices plotted in the figures above have an average peak power efficiency of 2.2%. This is more than double that of any previously reported NIR QD-LED (emitting beyond 1 μm) [54] and is comparable with those of commercial inorganic NIR LEDs ($\sim 3\text{-}15\%$ [55, 56]). These devices are representative of the devices produced over multiple months, although one anomalous but stable set of core-shell QD-LEDs demonstrated EQEs up to 9.4%. On the other hand, the EQEs of core-only QD-LEDs were consistently less than 1%.

4.4 Linking EQE and PL quantum yield

To understand the origin of the dramatic EQE improvement seen when core-only PbS QDs are replaced by core-shell PbS/CdS QDs in QD-LEDs, it is first noted that EQE

is a product of multiple effects:

$$EQE = \eta_r \cdot \chi \cdot \eta_{PL} \cdot \eta_{oc} \quad (4.2)$$

where η_r is the fraction of injected charges that form excitons in QDs, χ is the fraction of excitons whose states have spin-allowed optical transitions, η_{PL} is the QD PL QY resulting from these transitions, and η_{oc} is the fraction of emitted photons that are coupled out of the device (oc = “outcoupling”). Of these 4 variables, the addition of a CdS QD shell is most likely to significantly affect η_r (e.g. by increasing the efficiency of exciton generation) and/or η_{PL} (e.g. by passivating excitons generated in the PbS cores from external quenching mechanisms). The latter is a more accessible variable to probe via well-established techniques such as steady-state PL measurements, and such measurements are the focus of the remainder of this section.

η_{PL} of micron-thick drop-cast films of core-only PbS QDs and core-shell PbS/CdS QDs of varying shell thickness are measured using an integrating sphere and calibrated reference detectors [57]. These measurements reveal a ~ 2 -fold enhancement in η_{PL} – from 9.7% to 22% – upon the initial formation of a 0.18 nm CdS shell (the thinnest shell used in this series) and continued slight enhancement with increasing shell thickness, with η_{PL} reaching 33% for QDs with a 0.69-nm-thick shell (the thickest shell used in this series). While these results confirm that the growth of a CdS shell via cation exchange boosts the η_{PL} of QDs, they cannot account for the much more dramatic increase in EQE seen in QD-LEDs when core-only dots are replaced by core-shell ones.

However, unlike the QDs in a bulk drop-cast film, the QDs in a QD-LED structure are subject to PL quenching mechanisms, such as energy transfer to conductive neighboring layers, exciton dissociation at QD/charge transport layer interfaces, and Auger (non-radiative) recombination [28, 58, 59, 60]. Thus, the *in situ* η_{PL} of QDs in a QD-LED structure is likely very different from the η_{PL} of QDs in a drop-cast film. The relative η_{PL} of QDs in glass/ZnO/QD/CBP and glass/ZnO/QD structures that replicate the QDs *in situ* environment in a QD-LED are measured to provide a more

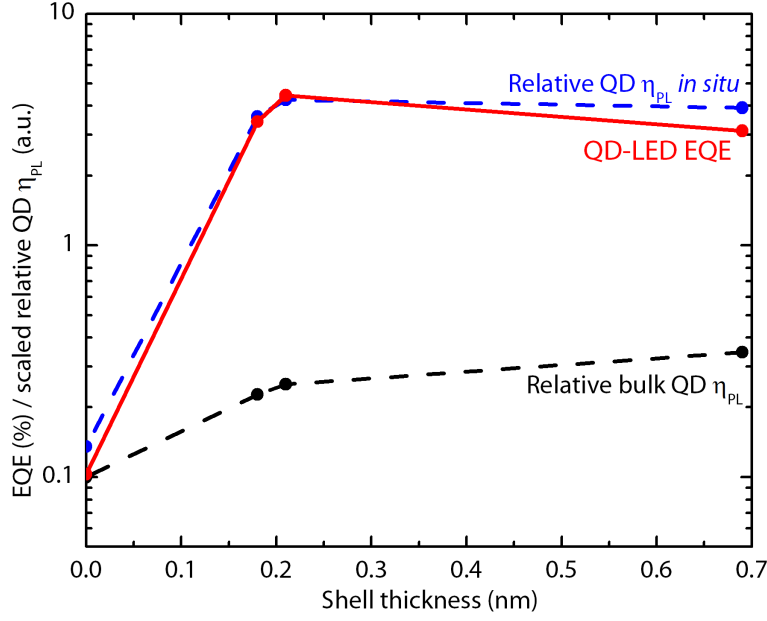


Figure 4-6: External quantum efficiencies (red) for QD-LEDs made with various QDs (including core-only and core-shell QDs with varying shell thickness) overlaid on trends in relative η_{PL} measured for bulk QD films (black) and for 8 nm QD films sandwiched between ZnO and CBP (blue).

relevant metric for evaluating the CdS shell's role in influencing η_{PL} . Relative η_{PL} is found by comparing the integrated areas under the QDs steady-state PL spectra. PL is measured in a fixed geometry setup to allow accurate comparisons in intensity among samples. The hermetically sealed (using Torr Seal ultra-high-vacuum epoxy) film stacks are optically excited with a 635 nm diode laser, which excites the QDs but is not appreciably absorbed by the ZnO and CBP layers. A low laser intensity of 0.5 mW/cm² is used such that steady-state PL does not decay with time (due to irreversible photobleaching). Emission is collected through an 850 nm long-pass filter with a Princeton Instruments Spectra Pro 300i spectrometer coupled to a liquid nitrogen-cooled Princeton Instruments OMA V InGaAs CCD array detector.

The calculated relative η_{PL} of these QDs *in situ* and the scaled η_{PL} of drop-cast QD films on glass are overlaid on the average peak EQEs for the corresponding QD-LEDs in Figure 4-6. Like EQE, the *in situ* relative η_{PL} increases by 1-2 orders of magnitude with the addition of a CdS shell, and for all QDs studied, the *in situ* relative η_{PL} roughly follows the trend in average peak EQE for the corresponding

QD-LEDs. This suggests that the high efficiencies of the QD-LEDs reported here is likely predominantly a result of boosting the *in situ* η_{PL} of the QDs. This dramatic improvement in *in situ* η_{PL} between core-only and core-shell QDs indicates that the CdS shell plays a significant role in protecting PbS QDs against significant non-radiative pathways present in the device. Test structures with and without CBP showed very similar trends, implying that ZnO (the more conductive charge transport layer), not CBP, is the layer largely responsible for the PL quenching in these QD-LEDs. Some possible mechanisms for this quenching are non-radiative energy transfer from visible QDs to plasmon modes in ZnO [28], electron transfer from PbS QDs to ZnO [58], or hole transfer to ZnO mid-gap states.

4.5 Summary

This chapter presents the development of record-efficiency NIR QD-LEDs by combining a modern, inorganic-QD-organic hybrid device architecture with the use of PbS/CdS core-shell QDs. This work demonstrates an increase in EQE of 1-2 orders of magnitude when core-only PbS QDs are replaced by core-shell PbS/CdS QDs. Correlation between EQE and relative QD PL quantum yield of devices with QDs of various shell thicknesses suggests that the EQE enhancement observed is largely due to the role of the shell in passivating the emissive QD cores against *in situ* PL quenching from the neighboring ZnO layer. These devices are arguably one of the first viable low-cost infrared light sources, and further improvements promise to pave the way for novel NIR applications.

Chapter 5

Optimization of Charge Transport Layers in QD-LEDs

Chapter 4 demonstrated the performance enhancement obtained by replacing core-only QDs with core-shell QDs and using a modern inorganic-QD-organic device architecture. This chapter details studies regarding the non-QD layers of this QD-LEDs structure – i.e. the electron transport, hole transport, and hole injection layers – to begin to understand how to stabilize and further boost QD-LED performance. Section 5.1 describes methods for producing stable films of zinc oxide (ZnO), the electron transport layer (ETL) deposited between the indium tin oxide (ITO) cathode and the emissive QD layer. Section 5.2 describes the material selection and thickness optimization of the organic small molecule hole transport layer (HTL) that is deposited on top of the QD layer. Finally, Section 5.3 demonstrates the critical role of a thin MoO_x hole injection layer (HIL) between the HTL and metal anode of a QD-LED in forming a working device.

5.1 Electron transport layer

Utilizing ZnO as the ETL of inorganic-QD-organic hybrid QD-LEDs has yielded the QD-LEDs with the highest reported performance in literature [51, 20], and attempts to use alternative metal oxides or organic layers for the QD-LED ETL in ONE Lab

have not been successful to date. ZnO may be deposited by vacuum deposition techniques, such as sputtering and atomic layer deposition (ALD), or solution processing techniques, such as sol-gel processing from zinc acetate and spin-casting ZnO nanoparticles. In radio-frequency (RF) sputtering, argon gas flowing through a low pressure (~ 100 mTorr) chamber is ionized by a 13.56 MHz alternating voltage that is applied between the desired target (in this case, ZnO) and the sputtering chamber. Ions bombarding the target and eject particles, which sputter ballistically and deposit onto a substrate suspended inside the chamber. Sputtering is generally considered a relatively reproducible process, especially when a sputtering system is connected to nitrogen-filled gloveboxes via a vacuum line as it is in ONE Lab, eliminating the effects of air exposure to the device during fabrication. Nonetheless, QD-LEDs produced in ONE Lab appear to only work with a specific ZnO target that was exhausted in 2011, and even fresh targets from the same manufacturer produce QD-LEDs that are very resistive and fail to turn on. It is possible that the single working target had conductive impurities that helped establish the electron transport/hole blocking characteristics required for QD-LEDs. However, attempts to intentionally dope ZnO with Sn during sputtering failed to reproduce the well-defined optical and electrical turn-on, in addition to $\geq 1\%$ EQEs, seen in legacy devices.

A few alternative processing techniques for depositing thin films of ZnO are sol-gel processing from zinc acetate and spin-casting ZnO nanoparticles. The latter technique has been used to produce the most efficient QD-LEDs reported to date [20], but preliminary efforts in ONE Lab to reproduce the reported results using ZnO nanoparticles fail to produce electroluminescent QD-LEDs. On the other hand, sol-gel processing produces smooth (<2 nm RMS roughness) ZnO films that can be used to make devices with EQEs above 4%, as demonstrated in the previous chapter. To produce such films, a zinc acetate [Zn(ac)] solution is prepared by stirring 12.56 g of zinc acetate dehydrate into 76.8 mL of 2-methoxyethanol (anhydrous) and 3.2 mL of ethanolamine (anhydrous) in an ambient nitrogen environment (Appendix A). It is then placed in an ultrasonic bath for approximately 5-6 hours. When making devices, the required amount of solution is first filtered through a $0.45\ \mu\text{m}$ mesh PTFE filter,



Figure 5-1: Image of dry-air-filled glovebag used to anneal ZnO during sol-gel processing.

and the filtered solution is spun cast onto an oxygen-plasma-cleaned ITO substrate at 2000 rpm in a glovebox. Spinning may also be done in outside the glovebox in air, but this makes processing susceptible to variations in ambient air temperature and humidity. Next, the samples are transferred to a glovebag filled with dry air (10% relative humidity), where they are annealed on a hotplate at 300°C for 5 minutes. This setup is shown in Figure 5-1. Oxygen is needed for ZnO to form during this process; when devices are annealed inside the glovebox, where the O₂ level is <0.1 ppm, they fail to electroluminesce. Dry air is used for annealing to make the process as repeatable as possible. ZnO is known to be sensitive to humidity, and several reports of ZnO humidity sensors have taken advantage of this property [61]. Unfortunately, this property is deleterious for QD-LEDs, as evidenced by the fact that annealing in ambient air – very humid during Boston summers – leads to optically rough films that produce inconsistent devices.

5.2 Hole transport layer

5.2.1 The “matted” phenomenon

4,4'-N,N'-dicarbazolebiphenyl (CBP) has been used as the standard HTL for QD-LEDs in ONE Lab since 2011, largely due to a combination of its availability/cost and success in producing high-performance QD-LEDs [51]. However, CBP is known

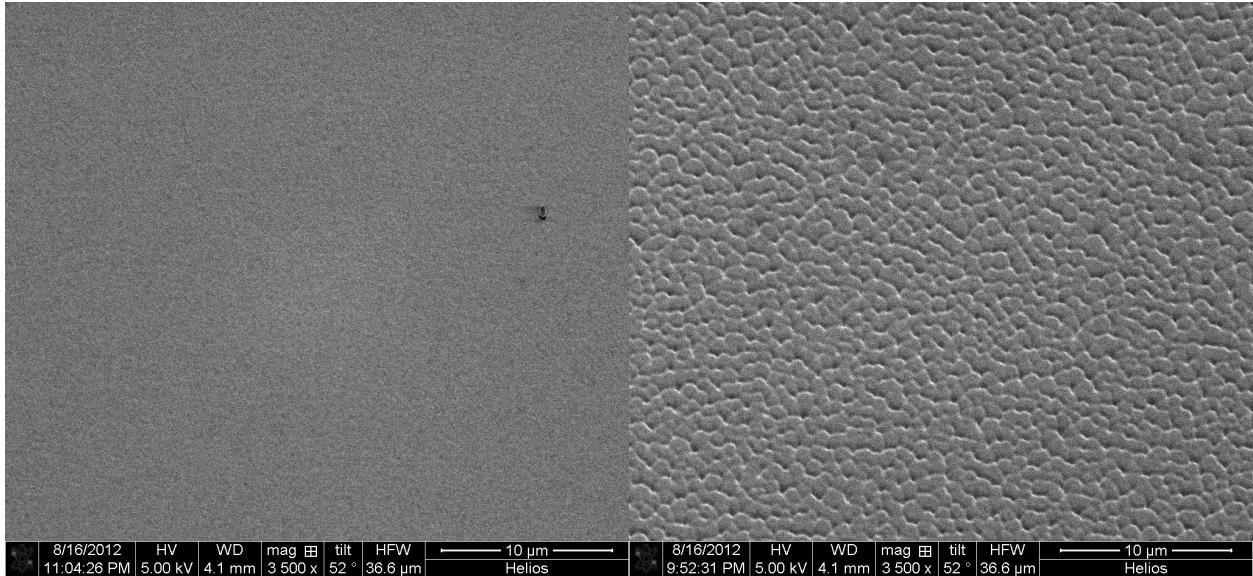


Figure 5-2: Surface of top gold electrode of a “normal” NIR QD-LED (left) and a “matted” NIR QD-LED (right).

to crystallize over time, leading to the formation of “islands” instead of a flat thin film. Figure 5-2 shows scanning electron micrographs of the surface of the top gold electrode of two QD-LEDs. In the image on the left, the gold film appears smooth. This device operates as expected. On the other hand, in the image on the right, the gold film is characterized by a leathery appearance with visible folds appearing on a micron scale. This device fails to optically turn on under an applied bias.

Figure 5-3 and Figure 5-4 show the cross sections of the above devices. The cross sections are prepared by focused ion-beam milling (FIB) a rectangular area with the sample tilted 52° , and the scanning electron micrographs are captured using a high-resolution magnetic immersion lens. These cross sections suggest that the “matted” appearance of the gold electrodes in the device on the right originates from the partial formation of islands in the CBP layer. While these 2 devices were made on different occasions, they were treated as identically as possible, with CBP, MoO_x , and Au thermally evaporated sequentially with as little time between each deposition as possible. The fact that the device on the right appeared matted immediately upon completion implies that the timescale for CBP island formation is very short.

Interestingly, this morphological phenomenon appears exclusively when CBP is

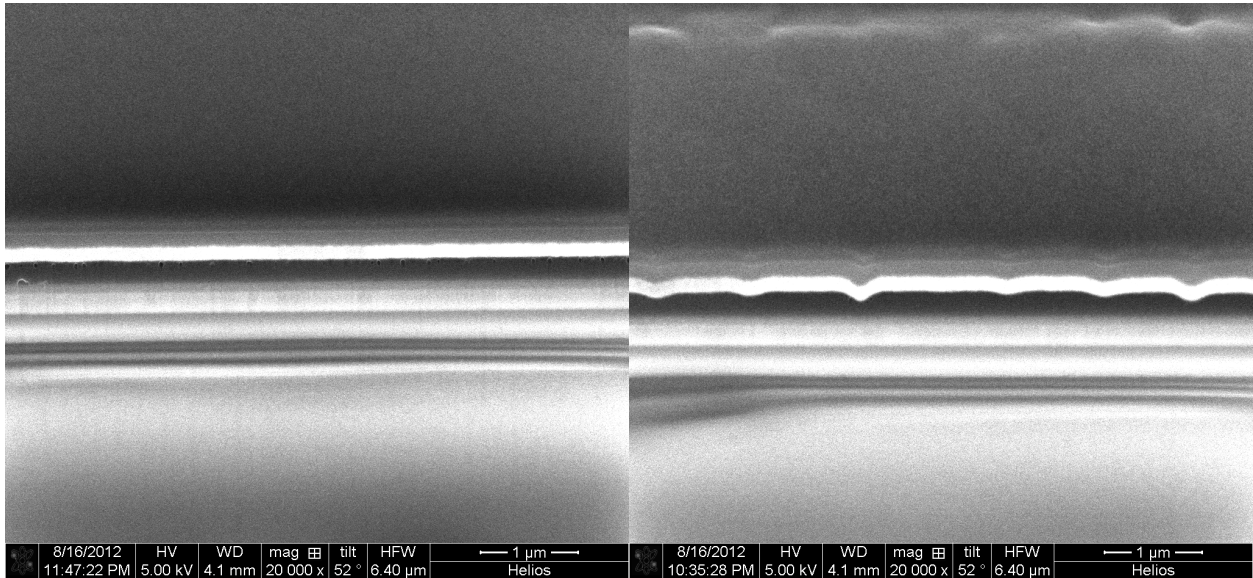


Figure 5-3: Cross sections of a “normal” NIR QD-LED (left) and a “matted” NIR QD-LED (right).

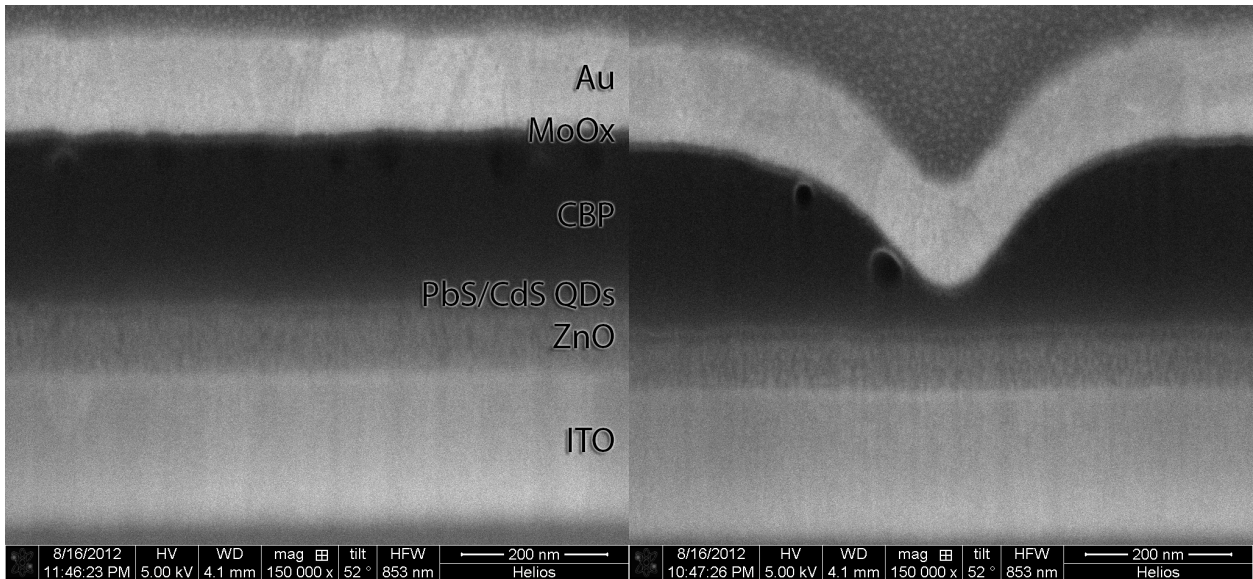


Figure 5-4: Zoomed-in cross sections of a “normal” NIR QD-LED (left) and a “matted” NIR QD-LED (right) showing that the roughness of the latter originates from the impartial formation of CBP islands.

deposited onto a QD layer (either core-only or core-shell); when deposited onto ZnO, no matted or cloudy appearance is observed. One possible explanation is that there is an unfavorable interaction between CBP molecules and the oleic acid QD ligands that discourages CBP film formation during deposition. It is unclear why the matted phenomenon only appears in some and not all devices.

5.2.2 Material selection

The instability of CBP films largely motivates the search for alternative materials for the HTL in QD-LEDs. One option for boosting the stability of QD-LEDs is to replace the organic HTL with an inorganic one. Indeed, reports of all-inorganic QD-LEDs that replace the organic HTL with a metal oxide one have been made, but these devices suffer from low EQEs (<0.1%) and low brightnesses (<2000 Cd/m²), probably because metal oxides generally quench the emissive QDs to a much greater extent than the less conductive organic molecule films do [28].

As a preliminary investigation of the effect of using different HTLs, pentacene and spiro-TPD, both materials with a HOMO 5 eV below the vacuum level (CBP has a HOMO of 6.3 eV), are tested as possible alternatives to CBP. MoO_x, which has a work function of 5.7 eV, is also tested. An inorganic-QD-organic hybrid QD-LED was made from a pre-patterned ITO cathode, a sol-gel ZnO (\sim 40 nm) ETL, a core-shell PbS-CdS QD layer (\sim 10 nm), various thermally evaporated HTLs (all 100 nm), a thermally evaporated MoO_x HIL, and a thermally evaporated Au (100 nm) anode. In this experiment, the devices with CBP showed less intense electroluminescence than expected for unknown reasons (again demonstrating the motivation to select an alternate material).

The current density vs. voltage ($J - V$) curves for these devices are shown in Figure 5-5. Despite the suppressed electroluminescence in the CBP control device, the $J - V$ curves for this device show rectifying behavior (i.e. electrical “turn-on”), although the slope of the on-state is lower than a typical electroluminescent device. The QD-LED with a spiro-TPD HTL exhibited significantly lower current both before and after turn-on, possibly due to a lower hole mobility in spiro-TPD compared to

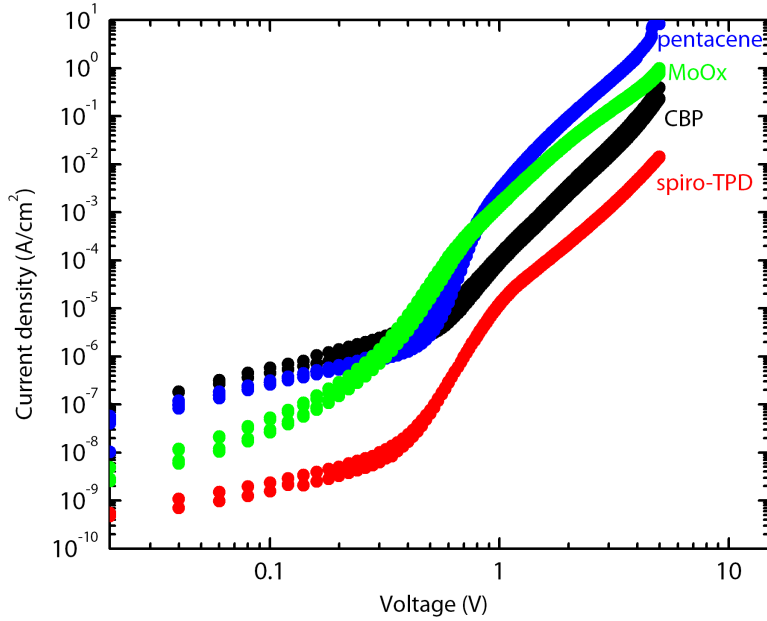


Figure 5-5: Current density versus voltage curves for QD-LEDs made with different HTLs (each is 100 nm thick).

the other HTLs.

Figure 5-6 shows the photodetector current (proportional to light output power, L) vs. voltage for these devices. From this plot, the QD-LED with a pentacene HTL shows a markedly lowered turn-on voltage of ~ 0.7 V (measured at a photodetector current of 10^{-10} A), surprisingly lower than the ~ 1 eV QD optical band-gap. The device with a MoO_x HTL also shows a low turn-on voltage of ~ 1 V, though the maximum light output power (observed at 4 V) is approximately 1 order of magnitude below that of the pentacene device. Finally, the device with a spiro-TPD HTL shows a turn-on voltage of ~ 1.5 V, comparable to what would be expected from a typical control QD-LED with a CBP HTL. From this figure, one might conclude that pentacene and MoO_x can more efficiently inject holes into QDs than spiro-TPD or CBP can and are promising alternatives to CBP. These results also suggest that flat band energy level alignment alone is insufficient in predicting charge injection efficiency and turn-on voltage, as pentacene and spiro-TPD in theory have comparable HOMO levels but clearly produce very different QD-LEDs when used in a device.

Figure 5-7 plots the EQE vs. current density of the QD-LEDs with different

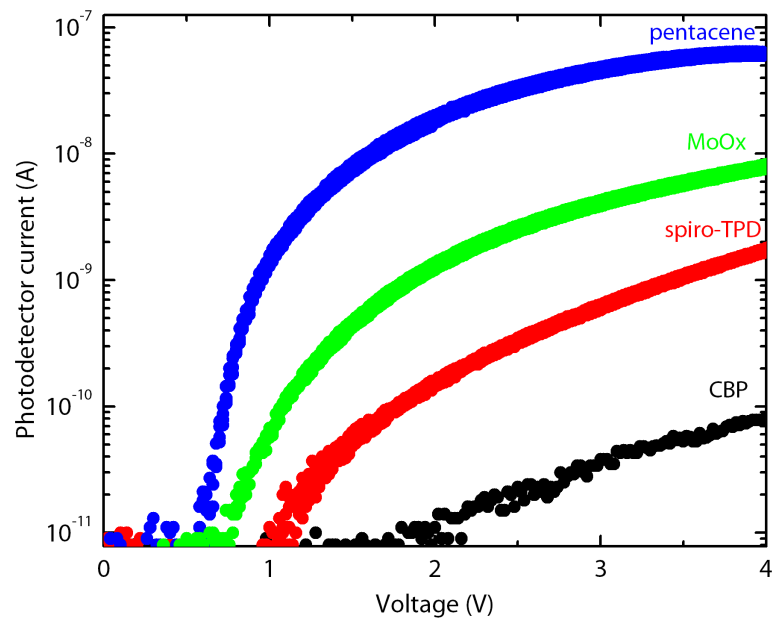


Figure 5-6: Photodetector current versus voltage for QD-LEDs made with different HTLs (each is 100 nm thick).

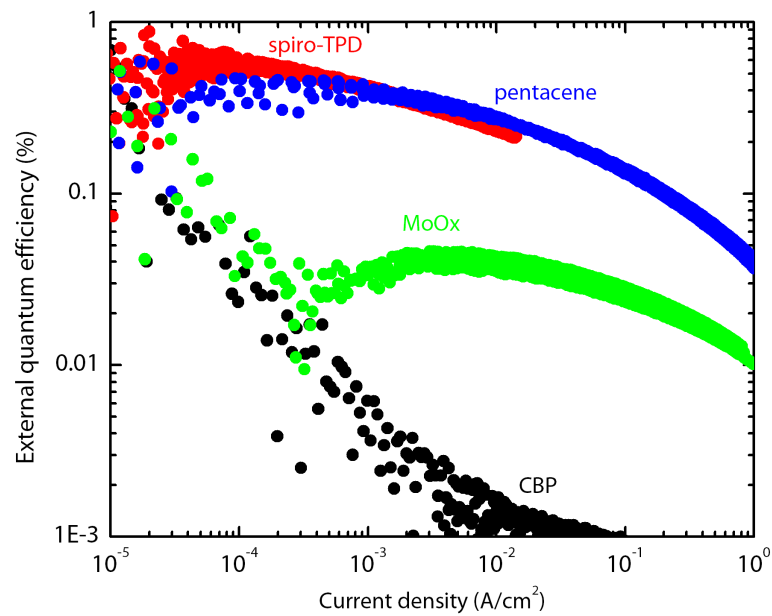


Figure 5-7: EQE versus current density for QD-LEDs made with different HTLs (each is 100 nm thick).

HTLs. The noticeably low photodetector current of the CBP control device seen in the previous figure is manifested here as very low (<0.01%) EQE. The QD-LEDs with spiro-TPD and pentacene HTLs both exhibited peak EQEs of $\sim 0.7\%$, a respectable value but 3-4 times lower than what would be expected from a typical QD-LED with CBP. The QD-LED with a MoO_x HTL exhibited a low peak EQE of 0.04%, consistent with the previously-reported low EQE of QD-LEDs with all-inorganic charge transport layers [28].

Although none of the HTL options tested in this experiment are definitively proven to be a good replacement for CBP in QD-LEDs, the promising sub-band-gap turn-on, high brightnesses, and respectable EQE seen in devices with a pentacene HTL suggests that unsurprisingly, there are indeed alternative materials that can be used to replace CBP in the current QD-LEDs made in ONE Lab. In fact, recent experiments not detailed here show that spiro-2-NPB is an HTL that leads to consistently shiny (non-matted) QD-LEDs with efficiencies and brightnesses comparable to, and sometimes even higher, than those of QD-LEDs with a CBP HTL. Such a material may pave the way for higher-performance, more stable QD-LEDs.

5.2.3 Microcavity effect

The reflective top electrode of a QD-LED allows the device to be modeled as a weak microcavity. This effect has been extensively studied and modeled in OLED literature, where it has been reported that changing the thicknesses of the organic layers in OLEDs can tune the intensity and wavelength of the EL spectrum measured at the device's surface normal [62, 63]. The enhanced EL intensity obtained from an optimized LED microcavity (i.e. that in which the path length of the photon is $\sim \frac{\lambda}{4}$) should in theory correlate with enhanced brightnesses and efficiencies.

To explore the possibility of this microcavity effect in QD-LEDs, 3 kinds of test structures are fabricated: (1) a “control” device comprising an ITO cathode, a ~ 40 nm ETL ZnO (sol-gel processed as described above), a ~ 10 nm PbS-CdS spun-cast QD layer, a 100 nm HTL CBP layer, a 10 nm MoO_x HIL layer, and finally a 100 nm reflective Au anode; (2) a device in which the CBP layer thickness is increased from

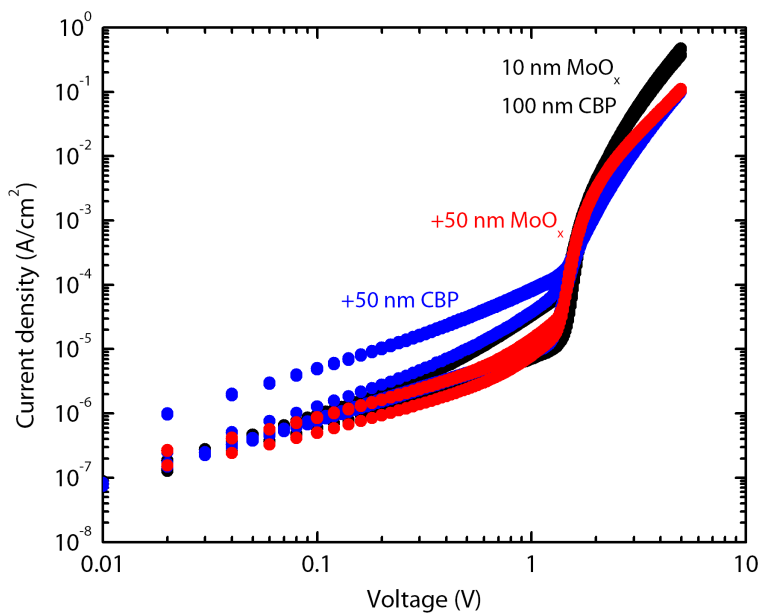


Figure 5-8: Current density versus voltage curves for QD-LEDs made with: a 100 nm CBP HTL + 10 nm MoO_x HIL (black), a 150 nm CBP HTL + 10 nm MoO_x HIL (blue), and a 100 nm CBP HTL + 60 nm MoO_x HIL (red).

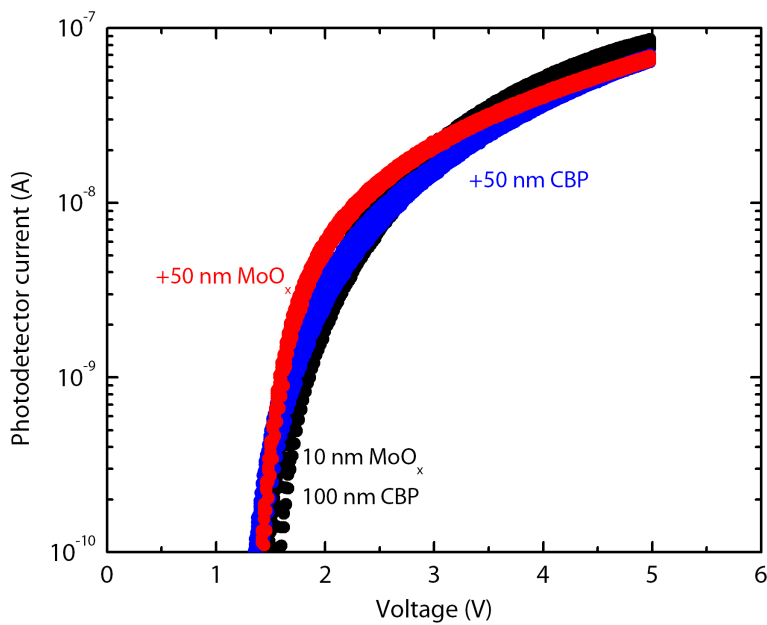


Figure 5-9: Photodetector current versus voltage curves for QD-LEDs made with: a 100 nm CBP HTL + 10 nm MoO_x HIL (black), a 150 nm CBP HTL + 10 nm MoO_x HIL (blue), and a 100 nm CBP HTL + 60 nm MoO_x HIL (red).

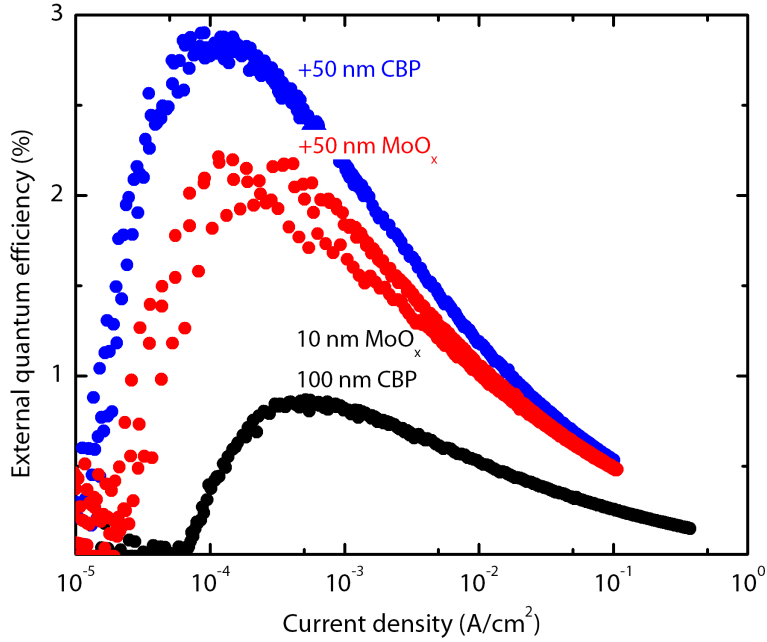


Figure 5-10: External quantum efficiency versus current density for QD-LEDs made with: a 100 nm CBP HTL + 10 nm MoO_x HIL (black), a 150 nm CBP HTL + 10 nm MoO_x HIL (blue), and a 100 nm CBP HTL + 60 nm MoO_x HIL (red).

100 nm to 150 nm; and (3) a device in which the MoO_x layer thickness is increased from 10 nm to 60 nm. The current density vs. voltage, photodetector current (proportional to light output power) vs. voltage, and EQE vs. current density curves for these devices are shown in Figure 5-8, Figure 5-9, and Figure 5-10, respectively. The most striking feature is the increase in EQE obtained from increasing the thicknesses of the layers between the electrodes – two-fold when the MoO_x layer is increased by 50 nm and three-fold when the CBP layer is increased by 50 nm. This significant enhancement suggests that further quantification and optimization of the microcavity effect in QD-LEDs is a promising potential avenue for increasing the efficiency of these devices. However, it must be noticed that increasing the thickness of CBP and/or MoO_x affects more than just the length of the QD-LED microcavity. Charge transport in the device is also affected, with an expected decrease in hole current as CBP thickness increases (the high conductivity of MoO_x means that this effect is smaller when increasing the thickness of the MoO_x HIL instead of the CBP HTL). This could play a role in optimizing the balance of electron and hole currents through the QD

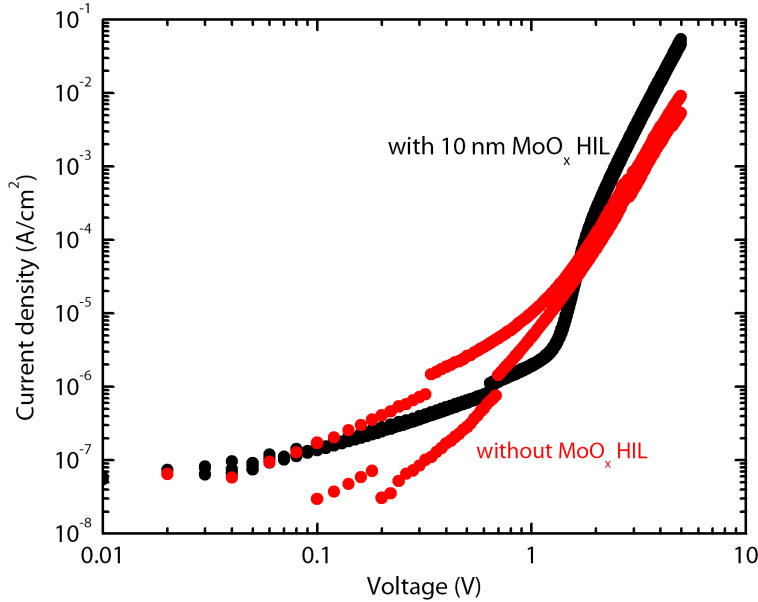


Figure 5-11: Current density versus voltage curves for QD-LEDs made with a 10 nm MoO_x HIL (black) and without one (red).

layer. Furthermore, it is possible that the efficiency enhancement could be explained merely by the fact that increasing the thickness of the CBP and/or MoO_x layers ameliorates the aforementioned “matted” phenomenon seen in some non-operational QD-LEDs. Nonetheless, it would be useful to model the microcavity effect so that the observed enhancement can be better understood and controlled.

5.3 Hole injection layer

MoO_x is cited in literature as an excellent hole injection layer that significantly improves performance in OLEDs [64, 65, 66]. To test the significance of a MoO_x in QD-LEDs, control QD-LEDs with the same structure as in the previous section (a pre-patterned ITO cathode, a ~ 40 nm ETL ZnO (sol-gel processed as described above), a ~ 10 nm PbS-CdS spun-cast QD layer, a 100 nm HTL CBP layer, a 10 nm MoO_x HIL layer, and a 100 nm Au anode) are fabricated along with otherwise identical QD-LEDs without the MoO_x HIL.

The current density vs. voltage, photodetector current (proportional to light output power) vs. voltage, and EQE vs. current density curves for these 2 types of

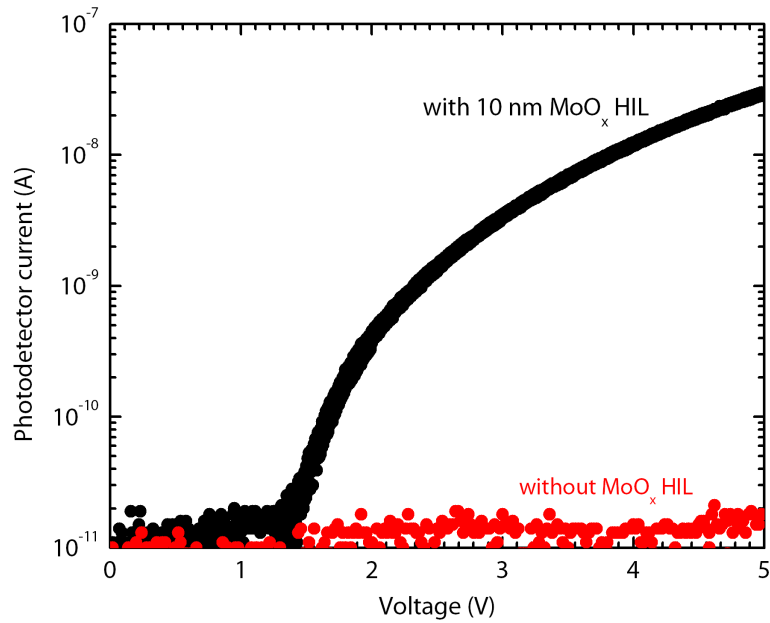


Figure 5-12: Photodetector current versus voltage curves for QD-LEDs made with a 10 nm MoO_x HIL (black) and without one (red).

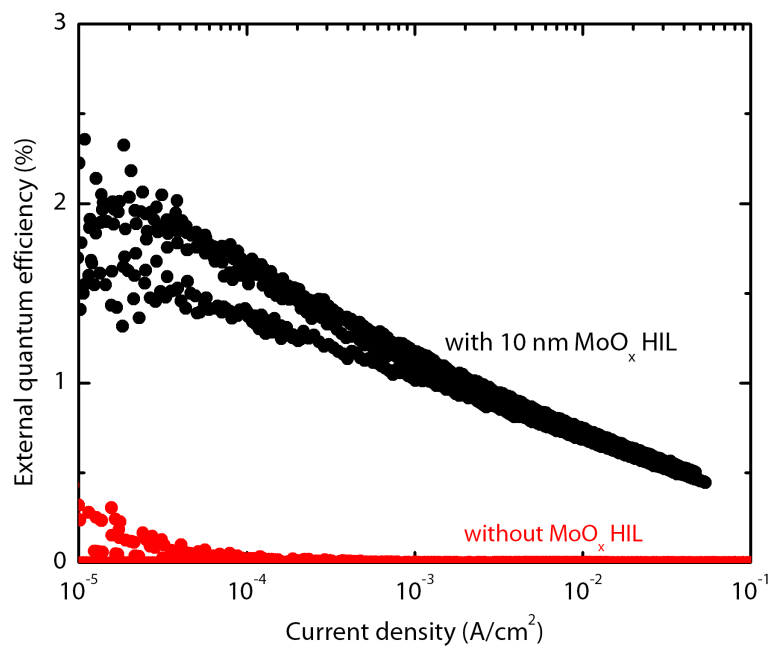


Figure 5-13: External quantum efficiency versus current density for QD-LEDs made with a 10 nm MoO_x HIL (black) and without one (red).

QD-LEDs are shown in Figure 5-11, Figure 5-12, and Figure 5-13, respectively. Figure 5-11 reveals a lack of electrical rectifying behavior (turn on) in the QD-LEDs without MoO_x (the discontinuities in the curve for the QD-LED without MoO_x are a result of the Keithley inappropriately switching sensitivity ranges and do not reflect any actual discontinuity in the device characteristics). Problematic behavior is further seen in Figure 5-11, which shows that without a MoO_x hole injection layer, QD-LEDs fail to electroluminesce. As a result, the EQEs of QD-LEDs made without MoO_x are extremely low, as seen in Figure 5-13.

5.4 Summary

This chapter explores various ways in which the charge transport layers in an inorganic-QD-organic hybrid QD-LED device structure can be modified to optimize device performance. First, the technique and processing conditions of ZnO , the metal oxide electron transport layer used here, are shown to play a critical role in device performance and consistency, and to date, sol-gel processing in dry air appears to be the most reliable method of producing reliable ZnO films. Likewise, the species and thickness of the organic hole transporting layer on the other side of the QD layer dramatically influence the turn-on voltage and EQE of QD-LEDs. Pentacene, spiro-TPD, and MoO_x are tested as possible alternatives in this thesis, and while none of these options appears to be a satisfactory replacement for CBP, promising signs suggest that a more suitable alternative may be found. Increasing the thickness of the CBP HTL and/or MoO_3HIL are shown to enhance EQE by 2-3 times, possibly thanks to a combination of better film coverage, a weak microcavity effect, and more balanced electron-hole charge transport. Finally, this thesis demonstrates the critical role of a thin (10 nm) MoO_3 HIL in allowing electroluminescent devices to be fabricated. Taken together, this chapter shows that in addition to the QD layer that is the focus of Chapters 3 and 4, there is much future work to be done to optimize and understand the charge transport layers surrounding the QDs in QD-LEDs.

Chapter 6

Conclusion

This thesis explores potential avenues of optimization to make efficient quantum dot light-emitting devices with core-shell quantum dots. The “baseline” device is an inorganic-QD-organic hybrid QD-LED architecture in which an emissive, core-shell QD layer is sandwiched between a metal oxide electron transporting layer and an organic small molecule hole transporting layer. This device structure has produced the most efficient QD-LEDs to date. Chapters 3 and 4 detail experiments related to the emissive QD layer, while Chapter 5 offers possible alternative methods of enhancing QD-LED performance by tuning the charge transport/injection layers surrounding the QD layer.

In particular, Chapter 3 describes the development of a new fabrication technique for depositing the QD layer – specifically, a core-shell CdSe/ZnS layer – in QD-LEDs emitting red/orange light. Electrophoretic deposition is demonstrated as a viable alternative to spin casting for forming thin QD films for use in QD-LEDs. QD-LEDs fabricated with an electrophoretically deposited QD layer demonstrate efficiencies comparable to QD-LEDs with a spun-cast QD layer of comparable thickness, and the EPD devices show electroluminescence “turn-on” at voltages surprisingly lower than the optical band-gap of the QDs. This EPD technique should readily be extendible to QDs with similar surface chemistry, including infrared PbS/CdS QDs.

In Chapter 4, the significance of using core-shell QDs in place of core-only QDs for an inorganic-QD-organic QD-LED is explored through the development of record-

performance near-infrared QD-LEDs utilizing core-shell PbS/CdS QDs that possess efficiencies ~ 100 times higher than those of otherwise identical devices with core-only PbS QDs. Comparisons among the photoluminescence quantum yields – both in a bulk drop-cast film and *in situ* in a QD-LED – of the core-only versus core-shell QDs reveal that the shell plays a critical role in shielding the emissive QD cores from quenching originating from the neighboring ZnO electron transport layer.

Finally, Chapter 5 presents variations on the charge transport layers (i.e. the non-QD layers) in QD-LEDs that could play a significant role in further enhancing the efficiency of QD-LEDs. For core-shell NIR QD-LEDs, the investigation of different film formation techniques for the ZnO electron transport layer reveals that sol-gel ZnO yields brighter and more efficient devices than sputtered ZnO does. In addition, increasing the thickness of the CBP hole transport layer or MoO_x hole injection layer increases the peak EQE of the devices by 2-3 times, possibly due to better coverage of the underlying layers or a microcavity effect.

Future work that quantifies and manipulates the many observations described in this thesis could lead to a better understanding of the operation of QD-LEDs and the development of more efficient devices.

Appendix A

Detailed fabrication procedures

A.1 QD crash-out

1. 0.2 mL 1-butanol is added to 0.8 mL QD solution (~ 40 mg/mL) in a pre-weighed 5 mL glass vial.
2. 1.5 mL methanol is added to the vial.
3. Vial is centrifuged for 5 minutes at 3500 rpm.
4. Supernatant is poured off and the vial is left open to dry in a fume hood for \sim 5 minutes.
5. Dried precipitate is redissolved in 0.8 mL hexane and the above procedure is repeated.
6. Vial is left open to completely dry for 30 minutes.
7. Vials are weighed to obtain the mass of QDs present and redissolved in chloroform to obtain a solution of known concentration.

A.2 Cleaning substrates

1. 0.5" \times 0.5" glass slides with pre-patterned ITO electrodes (ITO \sim 150 nm thick) are purchased from Thin Film Devices Inc.

2. Substrates are scrubbed with soapy water (M90:H₂O 1:400 by volume) and rinsed with DI water.
3. Substrates sonicated for 5 minutes in DI water.
4. Substrates sonicated for 5 minutes again in fresh DI water.
5. Substrates sonicated for 2 minutes in acetone.
6. Substrates sonicated for 2 minutes again in fresh acetone.
7. Substrates boiled for 2 minutes in isopropanol.
8. Substrates boiled for 2 minutes again in fresh isopropanol.
9. Substrates oxygen-plasma-cleaned for 1 minute and immediately transferred into a nitrogen-filled glovebox.

A.3 Sol-gel processing of ZnO

The Zn(ac) solution is prepared by stirring 12.56 g of zinc acetate dehydrate into 76.8 mL of 2-methoxyethanol (anhydrous) and 3.2 mL of ethanolamine (anhydrous) in an ambient nitrogen environment. It is then placed in an ultrasonic bath for approximately 5-6 hours.

Forming films:

1. 40 μ L of filtered Zn(ac) (using a 0.45 μ m mesh PTFE filter) solution is spun-cast at 2000 rpm for 30 seconds onto the substrate in a glovebox.
2. Substrates are transferred without ambient air exposure to a glovebag flushed with dry air (relative humidity \sim 10%).
3. Substrates heated on 300°C hot plate in glovebag for 5 minutes.
4. Substrates transferred without ambient air exposure to glovebox.

5. ZnO on edges of substrate is scraped off with tweezers to allow good contact to the underlying ITO electrode during device testing.
6. 90 μL of methoxyethanol is dropped onto a substrate and, \sim 3 seconds later, is spun off for 15 seconds.
7. 90 μL of methanol is dropped onto a substrate and, \sim 3 seconds later, is spun off for 15 seconds.

A.4 Evaporation of HTL, HIL, and anode

Table A.1: Sublimation conditions (for QD-LED HTL, HIL, and anode)

Film	Dep. rate ($\text{\AA}/\text{s}$)	Boat position	Current (A)	ρ (g/cm^3)	z-fac.	Tooling
CBP	0.8-1.2	Right-middle	44	1.1	8.83	67.8%
MoO_x	1.0	Left-middle	24	4.7	1.0	103%
Au	1.0	Left-front	67	19.3	2.381	75%
Al	0.8-1.2	Right-back	24	2.73	1.08	75%

After formation of a QD film on the ZnO ETL, the partial devices are placed into a small vacuum chamber for 1 hour to allow excess solvent to evaporate. Next, the HTL and HIL are deposited via thermal sublimation/evaporation in a 6-boat chamber with large-area masks (the HIL mask is slightly smaller in area than the HTL mask to avoid the possibility of shorting pathways between the HIL and the ITO cathode) using settings similar to the typical ones listed in Table A.1. The metal anode is then thermally evaporated in the same chamber using an electrode shadow mask. Masks are exchanged between each evaporation in a nitrogen glovebox connected to the thermal evaporator via a vacuum transfer line.

Bibliography

- [1] Y. Shirasaki, G. J. Supran, M. G. Bawendi, and V. Bulović. Emergence of colloidal quantum-dot light-emitting technologies. *Nature Photonics*, 7:13–23, January 2013.
- [2] S. A. Van Slyke, C. H. Chen, and C. W. Tang. Organic electroluminescent devices with improved stability. *Applied Physics Letters*, 69(15):2160–2162, 1996.
- [3] J. Wang, Y. D. Jiang, J. S. Yu, S. L. Lou, and H. Lin. Low operating voltage bright organic light-emitting diode using iridium complex doped in 4,4'-bis[N-1-naphthyl-N-phenyl-amino]biphenyl. *Applied Physics Letters*, 91(13):131105, 2007.
- [4] Z. Sun, C. Wang, J. Yang, B. Zhao, and J. R. Lombardi. Nanoparticle metal-semiconductor charge transfer in ZnO/PATP/Ag assemblies by surface-enhanced raman spectroscopy. *Journal of Physical Chemistry C*, 112(15):6093–6098, 2008.
- [5] J. Meyer, A. Shu, M. Kröger, and A. Kahn. Effect of contamination on the electronic structure and hole-injection properties of MoO₃/organic semiconductor interfaces. *Applied Physics Letters*, 96(13):133308, 2010.
- [6] O. L. Nelson and D. E. Anderson. Potential barrier parameters in thin-film Al-Al₂O₃-metal diodes. *Journal of Applied Physics*, 37(1):77–82, 1966.
- [7] H. J. Round. A note on carborundum. *Electrical World*, 19:309–310, February 1907.
- [8] F. M. Steranka, J. Bhat, D. Collins, L. Cook, M. G. Crawford, R. Fletcher, N. Gardner, P. Grillot, W. Goetz, M. Keuper, R. Khare, A. Kim, M. Krames, G. Harbers, M. Ludowise, P. S. Martin, M. Misra, G. Mueller, R. Mueller-Mach, S. Rudaz, Y.-C. Shen, D. Steigerwald, S. Stockman, S. Subramanya, T. Trottier, and J. J. Wierer. High power LEDs technology status and market applications. *physica status solidi (a)*, 194(2):380–388, 2002.
- [9] C. W. Tang and S. A. VanSlyke. Organic electroluminescent diodes. *Applied Physics Letters*, 51(12):913–915, September 1987.
- [10] C. Adachi, M.A. Baldo, M.E. Thompson, and S.R. Forrest. Nearly 100% internal phosphorescence efficiency in an organic light emitting device. *Journal of Applied Physics*, 90(10):5048–5051, 2001.

- [11] Z. Shen, P. E. Burrows, V. Bulović, S. R. Forrest, and M. E. Thompson. Three-color, tunable, organic light-emitting devices. *Science*, 276(5321):2009–2011, 1997.
- [12] G. Gu, P. E. Burrows, S. Venkatesh, S. R. Forrest, and M. E. Thompson. Vacuum-deposited, nonpolymeric flexible organic light-emitting devices. *Opt. Lett.*, 22(3):172–174, Feb 1997.
- [13] S. Forrest, P. Burrows, and M. Thompson. The dawn of organic electronics. *Spectrum, IEEE*, 37(8):29 –34, aug 2000.
- [14] S. R. Forrest. The road to high efficiency organic light emitting devices. *Organic Electronics*, 4(23):45 – 48, 2003.
- [15] V. L. Colvin, M. C. Schlamp, and A. P. Alivisatos. Light-emitting diodes made from cadmium selenide nanocrystals and a semiconducting polymer. *Nature*, 370:354–357, August 1994.
- [16] Z. Tan, J. Xu, C. Zhang, T. Zhu, F. Zhang, B. Hedrick, S. Pickering, J. Wu, H. Su, S. Gao, A. Y. Wang, B. Kimball, J. Ruzylo, N. S. Dellas, and S. E. Mohney. Colloidal nanocrystal-based light-emitting diodes fabricated on plastic toward flexible quantum dot optoelectronics. *Journal of Applied Physics*, 105(3):034312, 2009.
- [17] T. Zhu, K. Shanmugasundaram, S. C. Price, J. Ruzylo, F. Zhang, J. Xu, S. E. Mohney, Q. Zhang, and A. Y. Wang. Mist fabrication of light emitting diodes with colloidal nanocrystal quantum dots. *Applied Physics Letters*, 92(2):023111, 2008.
- [18] V. Wood, M. J. Panzer, J. Chen, M. S. Bradley, J. E. Halpert, M. G. Bawendi, and V. Bulović. Inkjet-printed quantum dot–polymer composites for full-color AC-driven displays. *Advanced Materials*, 21(21):2151–2155, 2009.
- [19] L. Kim, P. O. Anikeeva, S. A. Coe-Sullivan, J. S. Steckel, M. G. Bawendi, and V. Bulović. Contact printing of quantum dot light-emitting devices. *Nano Letters*, 8(12):4513–4517, 2008.
- [20] B. S. Mashford, P. T. Kazlas, M. Stevenson, Z. Popovic, C. Hamilton, Z. Zhou, C. Breen, J. Steckel, V. Bulović, M. Bawendi, and S. Coe-Sullivan. Low-voltage and high-efficiency quantum dot light emitting device via optimized charge injection. *Nature Photonics*, 2013.
- [21] B. W. D’Andrade and S. R. Forrest. White organic light-emitting devices for solid-state lighting. *Advanced Materials*, 16(18):1585–1595, 2004.
- [22] S. H. Xin, P. D. Wang, A. Yin, C. Kim, M. Dobrowolska, J. L. Merz, and J. K. Furdyna. Formation of self-assembling CdSe quantum dots on ZnSe by molecular beam epitaxy. *Applied Physics Letters*, 69(25):3884–3886, December 1996.

- [23] C. B. Murray, D. J. Norris, and M. G. Bawendi. Synthesis and characterization of nearly monodisperse CdE (E = S, Se, Te) semiconductor nanocrystallites. *Journal of the American Chemical Society*, 115(19):8706–8715, September 1993.
- [24] S. M. Geyer, J. M. Scherer, N. Moloto, F. B. Jaworski, and M. G. Bawendi. Efficient luminescent down-shifting detectors based on colloidal quantum dots for dual-band detection applications. *ACS Nano*, 5(7):5566–5571, 2011.
- [25] B. O. Dabbousi, J. Rodriguez-Viejo, F. V. Mikulec, J. R. Heine, H. Mattoussi, R. Ober, K. F. Jensen, and M. G. Bawendi. (CdSe)ZnS core-shell quantum dots: Synthesis and characterization of a size series of highly luminescent nanocrystallites. *Journal of Physical Chemistry B*, 101(46):9463–9475, November 1997.
- [26] J. M. Pietryga, D. J. Werder, D. J. Williams, J. L. Casson, R. D. Schaller, V. I. Klimov, and J. A. Hollingsworth. Utilizing the lability of lead selenide to produce heterostructured nanocrystals with bright, stable infrared emission. *Journal of the American Chemical Society*, 130(14):4879–4885, 2008.
- [27] S. Coe, W.-K. Woo, M. Bawendi, and V. Bulović. Electroluminescence from single monolayers of nano crystals in molecular organic devices. *Nature*, 420:800–803, December 2002.
- [28] J. M. Caruge, J. E. Halpert, V. Wood, V. Bulović, and M. G. Bawendi. Colloidal quantum-dot light-emitting diodes with metal-oxide charge transport layers. *Nature Photonics*, 2:247–250, April 2008.
- [29] B. Kumar, R. Hue, W. L. Gladfelter, and S. A. Campbell. Comparing direct charge injection and Forster energy transfer into quantum dots in hybrid organic/inorganic quantum dot light emitting devices. *Journal of Applied Physics*, 112:034501, 2012.
- [30] P. O. Anikeeva, C. F. Madigan, J. E. Halpert, M. G. Bawendi, and V. Bulović. Electronic and excitonic processes in light-emitting devices based on organic materials and colloidal quantum dots. *Physical Review B*, 78:085434, 2008.
- [31] A. Rose. Space-charge-limited currents in solids. *Physical Review*, 97(6):1538–1544, 1955.
- [32] S. Coe-Sullivan, Z. Zhou, Y. Niu, J. Perkins, M. Stevenson, C. Breen, P. T. Kazlas, and J. S. Steckel. Quantum dot light emitting diodes for near-to-eye and direct view display applications. *SID Symposium Digest of Technical Papers*, 42(1):135–138, June 2011.
- [33] S. Coe-Sullivan. Nanotechnology for displays: A potential breakthrough for OLED displays and LCDs. Presented at SID Display Week 2012 (Seminar M-5), June 2012.

- [34] M. J. Panzer, V. Wood, S. M. Geyer, M. G. Bawendi, and V. Bulović. Tunable infrared emission from printed colloidal quantum dot/polymer composite films on flexible substrates. *Journal of Display Technology*, 6(3):90–93, Mar 2010.
- [35] O. O. Van der Biest and L. J. Vandeperre. Electrophoretic deposition of materials. *Annual Review of Materials Science*, 29(1):327–352, 1999.
- [36] L. Besra and M. Liu. A review on fundamentals and applications of electrophoretic deposition (EPD). *Progress in Materials Science*, 52(1):1 – 61, 2007.
- [37] M. A. Islam and I. P. Herman. Electrodeposition of patterned CdSe nanocrystal films using thermally charged nanocrystals. *Applied Physics Letters*, 80(20):3823 –3825, May 2002.
- [38] M. A. Islam, Y. Xia, D. A. Telesca, M. L. Steigerwald, and I. P. Herman. Controlled electrophoretic deposition of smooth and robust films of CdSe nanocrystals. *Chemistry of Materials*, 16(1):49–54, 2004.
- [39] Q. Zhang, T. Xu, D. Butterfield, M. J. Misner, D. Y. Ryu, T. Emrick, and T. P. Russell. Controlled placement of CdSe nanoparticles in diblock copolymer templates by electrophoretic deposition. *Nano Letters*, 5(2):357–361, 2005.
- [40] P. Brown and P. V. Kamat. Quantum dot solar cells. electrophoretic deposition of CdSe-C₆₀ composite films and capture of photogenerated electrons with nC₆₀ cluster shell. *Journal of the American Chemical Society*, 130(28):8890–8891, 2008.
- [41] A. Salant, M. Shalom, I. Hod, A. Faust, A. Zaban, and U. Banin. Quantum dot sensitized solar cells with improved efficiency prepared using electrophoretic deposition. *ACS Nano*, 4(10):5962, 2010.
- [42] N. J. Smith, K. J. Emmett, and S. J. Rosenthal. Photovoltaic cells fabricated by electrophoretic deposition of CdSe nanocrystals. *Applied Physics Letters*, 93(4):043504 –043504–3, jul 2008.
- [43] I. Horcas, R. Fernandez, J. M. Gomez-Rodriguez, J. Colchero, J. Gomez-Herrero, and A.M. Baro. WSxM: A software for scanning probe microscopy and a tool for nanotechnology. *Review of Scientific Instruments*, 78(1):013705, 2007.
- [44] C. A. Leatherdale and M. G. Bawendi. Observation of solvatochromism in CdSe colloidal quantum dots. *Physical Review B*, 63(16):165315, 2001.
- [45] C. R. Kagan, C. B. Murray, M. Nirmal, and M. G. Bawendi. Electronic energy transfer in CdSe quantum dot solids. *Physical Review Letters*, 76(9):1517–1520, 1996.
- [46] E. J. D. Klem, L. Levina, and E. H. Sargent. PbS quantum dot electroabsorption modulation across the extended communications band 1200–1700 nm. *Applied Physics Letters*, 87:053101, 2005.

- [47] Y. T. Lim, S. Kim, A. Nakayama, N. E. Stott, M. G. Bawendi, and J. V. Frangioni. Selection of quantum dot wavelengths for biomedical assays and imaging. *Molecular Imaging*, 2(1):50–64, 2003.
- [48] G. Qian, Z. Zhong, M. Luo, D. Yu, Z. Zhang, Z. Y. Wang, and D. Ma. Simple and efficient near-infrared organic chromophores for light-emitting diodes with single electroluminescent emission above 1000 nm. *Advanced Materials*, 21(1):111–116, 2009.
- [49] O. Chen, J. Zhao, V. P. Chauhan, J. Cui, C. Wong, D. K. Harris, H. Wei, H. S. Han, D. Fukumura, R. K. Jain, and M. G. Bawendi. Compact high-quality CdSe-CdS core-shell nano crystals with narrow emission linewidths and suppressed blinking. *Nature Materials*, 12, February 2013.
- [50] L. Sun, J. J. Choi, D. Stachnik, A. C. Bartnik, B.-R. Hyun, G. G. Malliaras, T. Hanrath, and F. W. Wise. Bright infrared quantum-dot light-emitting diodes through inter-dot spacing control. *Nature Nanotechnology*, 7:369–373, 2012.
- [51] J. Kwak, W. K. Bae, D. Lee, I. Park, J. Lim, M. Park, H. Cho, H. Woo, D. Y. Yoon, K. Char, S. Lee, and C. Lee. Bright and efficient full-color colloidal quantum dot light-emitting diodes using an inverted device structure. *Nano Letters*, 12(5):2362–2366, 2012.
- [52] M. V. Kovalenko, R. D. Schaller, D. Jarzab, M. A. Loi, and D. V. Talapin. Inorganically functionalized PbS-CdS colloidal nanocrystals: Integration into amorphous chalcogenide glass and luminescent properties. *Journal of the American Chemical Society*, 134(5):2457–2460, 2012.
- [53] J. Jasieniak, M. Califano, and S. E. Watkins. Size-dependent valence and conduction band-edge energies of semiconductor nanocrystals. *ACS Nano*, 5(7):5888–5902, June 2011.
- [54] K. N. Bouridakos, D. M. N. M. Dissanayake, T. Lutz, S. R. P. Silva, and R. J. Curry. Highly efficient near-infrared hybrid organic-inorganic nanocrystal electroluminescence device. *Applied Physics Letters*, 92(15):153311, 2008.
- [55] T. Kawazoe, M. A. Mueed, and M. Ohtsu. Highly efficient and broadband si homojunction structured near-infrared light emitting diodes based on the phonon-assisted optical near-field process. *Applied Physics B*, 104(4):747–754, 2011.
- [56] Roithner Lasertechnik GmbH, 2010.
- [57] S. M. Geyer, J. M. Scherer, N. Moloto, F. B. Jaworski, and M. G. Bawendi. Efficient luminescent down-shifting detectors based on colloidal quantum dots for dual-band detection applications. *ACS Nano*, 5(7):5566–5571, 2011.
- [58] P. R. Brown, R. R. Lunt, N. Zhao, T. P. Osedach, D. D. Wanger, L.-Y. Chang, M. G. Bawendi, and V. Bulović. Improved current extraction from ZnO/PbS

- quantum dot heterojunction photovoltaics using a MoO₃ interfacial layer. *Nano Letters*, 11(7):2955–2961, 2011.
- [59] Y.-W. Hyun, B.-R. and Zhong, A. C. Bartnik, L. Sun, H. D. Abruna, F. W. Wise, J. D. Goodreau, J. R. Matthews, T. M. Leslie, and N. F. Borrelli. Electron injection from colloidal PbS quantum dots into titanium dioxide nanoparticles. *ACS Nano*, 2(11):2206–2212, 2008.
 - [60] H. C. Leventis, F. OMahony, J. Akhtar, M. Afzaal, P. OBrien, and S. A. Haque. Transient optical studies of interfacial charge transfer at nanostructured metal oxide/PbS quantum dot/organic hole conductor heterojunctions. *Journal of the American Chemical Society*, 132(8):2743–2750, 2010.
 - [61] A. Erol, S. Okur, B. Comba, O. Mermer, and M. Ç. Arıkan. Humidity sensing properties of ZnO nanoparticles synthesized by sol-gel process. *Sensors and Actuators B: Chemical*, 145(1):174–180, March 2010.
 - [62] V. Bulović, V. B. Khalfin, G. Gu, P. E. Burrows, D. Z. Garbuzov, and S. R. Forrest. Weak microcavity effects in organic light-emitting devices. *Physical Review B*, 58(7):3730–3740, August 1998.
 - [63] R. H. Jordan, A. Dodabalapur, and R. E. Slusher. Efficiency enhancement of micro cavity organic light emitting diodes. *Applied Physics Letters*, 69(14):1997–1999, September 1996.
 - [64] M. Kroger, S. Hamwi, J. Meyer, T. Riedl, W. Kowalsky, and A. Kahn. Role of the deep-lying electronic states of MoO₃ in the enhancement of hole-injection in organic thin films. *Journal of Physics D: Applied Physics*, 29(11):2750–2753, 1996.
 - [65] S. Tokito, K. Noda, and Y. Taga. Metal oxides as a hole-injecting layer for an organic electroluminescent device. *Journal of Physics D: Applied Physics*, 29(11):2750–2753, 1996.
 - [66] H. You, Y. Dai, Z. Zhang, and D. Ma. Improved performances of organic light-emitting diodes with metal oxide as anode buffer. *Journal of Applied Physics*, 101(2):026105, 2007.